Supplementary Information

Gram-scale bottom-up flash graphene synthesis

Duy X. Luong,[1,2] Ksenia V. Bets,[3] Wala Ali Algozeeb,[2] Michael G. Stanford,[2] Carter Kittrell,[2] Weiyin Chen,[2] Rodrigo V. Salvatierra,[2] Muqing Ren,[2] Emily A. McHugh,[2] Paul A. Advincula,[2] Zhe Wang,[2] Mahesh Bhatt,[4] Hua Guo,[3] Vladimir Mancevski,[2] Rouzbeh Shahsavari,[4,5*] Boris I. Yakobson,[2,3,6*] and James M. Tour[2,3,6*]

[1]Applied Physics Program, [2]Department of Chemistry, [3]Department of Materials Science and NanoEngineering,

Rice University, 6100 Main Street, Houston, Texas 77005, USA

[4]C-Crete Technologies, 13000 Murphy Rd, Unit 102, Stafford, TX 77477, USA

[5]Department of Civil and Environmental Engineering, [6]Smalley-Curl Institute and the NanoCarbon Center,

Rice University, 6100 Main Street, Houston, Texas 77005, USA

Equipment

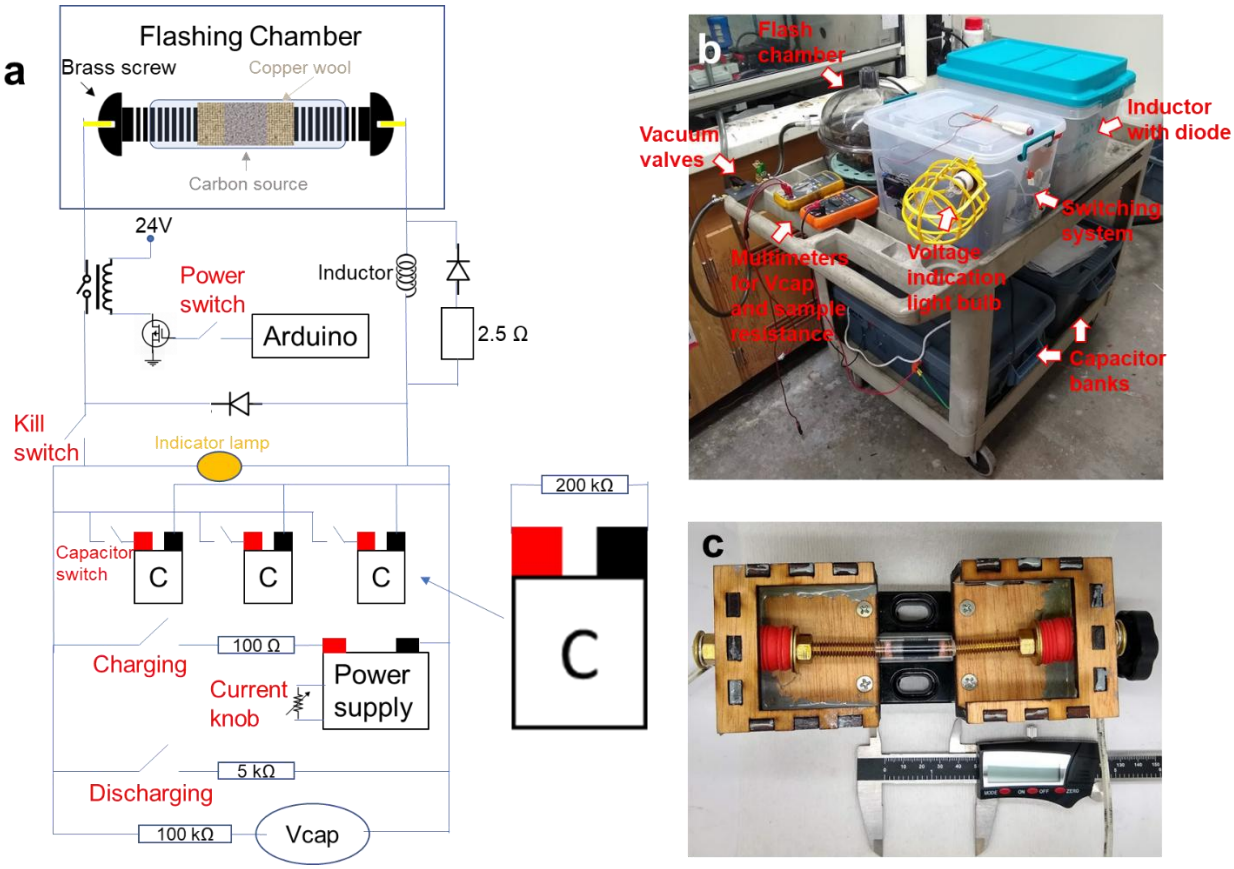

Supplementary Fig. 1. FJH system. **a**. Electrical schematic of the FJH system. **b**. Photograph of the system set up on a plastic cart. c. The sample holder that is made from a small commercial vise (Amazon) and laser cut wooden parts. The loosely fitting (to permit gas escape during flashing) brass screws act as two electrodes that contact the copper wool plugs (or graphite disks) that touch the desired carbon source. Red rubber stoppers provide gradual compressing of the

sample while the vice is compressed to increase the conductivity of the sample. Caliper width is 5 cm.

FJH Components list:

- Capacitor: 10x of 450 V, 6 mF aluminum electrolytic capacitors (Mouser #80-PEH200YX460BQU2). This capacitor bank is for FG synthesis with batch sizes ≤0.5 g
- 10x of 400 V, 18 mF aluminum electrolytic capacitors (Mouser # 80-ALS70A183QS400). This additional capacitor bank is for FG synthesis with batch sizes >0.5 g and up to 1.0 g
- Mechanical relay: 900 V, 500 A (TE Connectivity LEV200A5ANA)
- Power supply: LED Power Supplies 299.6W 214-428V 700mA (Mouser # 709-HLG320H-C700B). Current knob is a 10 kΩ potentiometer
- Vcap is measured by a multimeter Fluke 189
- Discharging and charging switch breaker: 400 V, 6A (ABB S 282 K 6A)
- Capacitor switch breaker: 277 V, 10 A (ABB S201P-C10)
- Kill switch breaker: 440 V, 63 A (AAB S283 UC Z 63A)
- Controller: Arduino Uno with LCD display
- Inductor: 24 mH (Mouser #553-C-80U)
- Diode: 1200 V, 560 A (Mouser #747-MDO500-12N1)

CAUTION: There is a risk of electrical shock or even electrocution, so these features should be implemented. This list is not intended to be comprehensive but demonstrative of the protocols needed to minimize risk.

1. Enclose or carefully insulate all wire connections.

2. All connections, wires and components must be suitable for the high voltages and currents.
3. Be aware that component failure could cause high voltage to appear in unexpected places, such as heat sinks on the switching transistors.
4. Control wires should have opto-isolators rated for high voltage.
5. Provide a visible charge indicator. A 230 V clear glass incandescent light bulb is a good choice as the glow on the filament also provides an approximate indicator of the amount of charge on the capacitor bank. Bright light = danger!
6. Do not use toggle switches with metal toggles. If an arc develops, the metal toggle could become charged.
7. One hand rule. Use only one hand when working on the system, with the other hand not touching any grounded surface.
8. Install bleed resistors in the range of 100,000 ohms on each capacitor so that charge will always bleed off in ~1 h.
9. Provide a mechanical discharge circuit breaker switch connected to a power resistor of a few hundred ohms to rapidly bleed off the capacitor charge.
10. Provide a "kill" circuit breaker switch to disconnect the sample holder from the capacitor bank.
11. Provide an AC disconnect circuit breaker switch.
12. Post high voltage warning signs on the apparatus.
13. Use of circuit breakers as switches. Circuit breakers have built-in arc suppression that can interrupt 1000 amps or more. Conventional switches do not have such a high level of arc suppression and can burn out or weld closed due to the high current pulses.

14. Use circuit breakers rated for DC voltage. Most AC circuit breakers have a DC rating 1/2 the voltage or less, since DC arcs are much more difficult to suppress. Circuit breakers designed for DC solar power systems are a good choice.
15. When choosing circuit breakers, choose by the time curves typical for 0.1 s, rather than the steady state current rating. K-type DC circuit breakers will have ~10x higher trip current at 0.1 s compared to their rated current, and Z-type breakers will have ~4x higher trip current at 0.1 s. This "delayed trip" designed into most circuit breakers will allow much higher pulse currents than the steady state rating of the breaker.
16. Include a small amount of inductance in the discharge circuit to limit the rise time to a millisecond or more. Extremely fast discharges can damage components and cause RF interference with other lab apparatus.
17. Keep in mind that the system can discharge many thousands of Joules in milliseconds, which can cause components such as relays or even capacitors to explode. These components should be enclosed to protect against both high voltage and possible flying debris.
18. Keep a voltmeter with high voltage test leads handy at all times. When working on the capacitor bank, always check the voltage on each. A broken wire or loose connection could leave the capacitor in a charged state.
19. Wear thick rubber gloves when using the apparatus to protect from electrocution.
20. All users should be properly trained by an experienced electrical technician.

Commercialization of laboratory-scale equipment will likely follow using these design and safety parameters.

Estimated energy for conversion of high carbon materials into FG:

With 100 mg batch, a bank of capacitors with capacitance of 60 mF discharge from 220 V – 150 V, then

$$E = \frac{({V_1}^2 - {V_2}^2) \times C}{2 \times M} = 7.2\ kJ \cdot g^{-1}$$

E: Energy per gram

V_1 and V_2: Voltage before and after flash, respectively

C: Capacitance

M: Mass per batch

Discussion of Raman Analyses and Turbostratic Graphene

Graphene is defined as a 2-D material

While graphene is often depicted as a single sheet of carbon, it occurs as a single isolated sheet only in specialized laboratory conditions. In any substantial production method such as we are reporting here, graphene will appear in the form of aggregates. The pioneers in this field have defined graphene as a 2-D material, in contrast to carbon nanotubes as a 1-D material and graphite as a 3-D material.[1, 2, 3, 4] When the sp^2-carbon sheets within these aggregates retain the electronic structure of a 2-D rather than 3-D material, then a descriptive adjective is used as a prefix, such as *bilayer graphene, few-layer graphene, N-layer graphene*. If AB-stacked (Bernal), then graphene is the term used when there are <10-layers since there are distinct physical properties, relative to graphite, at <10 layers. Only at >9 layers, do graphite-like property ensue and only if the adjacent sheets are AB-stacked.[5] When randomly oriented layering occurs rather than AB-stacked as in the case of FG, several different adjectives are used with the same meaning, such as: *misoriented*,[3] *twisted*,[6] *rotated*,[7] *rotationally faulted*,[8, 9] *weakly coupled*,[10] and

turbostratic.[11] In spite of the varied terminology, there is agreement among many authors that in these cases, the individual layers retain their 2-D properties when randomly stacked. Hence, the use of the term "*graphene*" for such stacking is supported in the scientific literature, even when there are many layers.[12] As we will show, the Raman spectrum provides a direct monitor for the electronic structure and is also unambiguous in identifying the 2-D nature of these aggregates.

It is not the physical dimensions or the number of atomic layers but rather the properties, especially electronic properties that constitute a 2-D material. Graphene is characterized by a 2-D gas of Dirac fermions.[13] A 2-D material is that which is highly anisotropic in electron mobility, just as carbon nanotubes are a 1-D material because high mobility in one direction. For graphene, the mobilities are ballistic in the x-y plane, but when stacked, the c-axis mobility is very much smaller. And turbostratic graphene has the greatest anisotropy of all, and even for multiple layers, it remains fully 2D with ballistic mobility in two dimensions, and many orders of magnitude lower conductivity in the third dimension.

Experimental measurements by Kim et al. demonstrate that the extremely large anisotropy between ballistic electrons in plane and those trying to cross between layers is retained when the graphene sheets are stacked in a twisted manner.[7] They report ~10^{-3} ohm-meter resistivity for highly ordered pyrolytic graphite (HOPG) which is ~5 orders of magnitude higher resistivity than copper and the interlayer resistivity is again 4 orders of magnitude larger. The in-plane transport for turbostratic graphene remains ballistic for the electrons. Turbostratic graphene, even with many layers, is truly a 2-D material whereby electrons move with complete freedom like a massless Fermi gas in two dimensions but are, in effect, unable to move perpendicular to the layering. It is rare to find any other material that is so purely 2D as multilayer turbostratic graphene.

Raman as a definitive standard for 2-D character

Raman spectroscopy has become the standard as a diagnostic of graphene; that tool appears in almost every experimental study.[4, 7, 8, 9, 12, 14, 15, 16, 17] And that is because it is a direct probe of the electronic band structure of the graphene, which in turn plays a central role in the unique character of this 2-D material.

Turbostratic graphite vs. turbostratic graphene

The D-peak of turbostratic graphite is much larger than both the G-peak and the 2D peak, which is opposite for an optimized sample of FG which has a D-peak that is very much smaller than the G-peak, which in turn is smaller than the 2D peak.[18] Raman spectroscopy is a probe of the vibrational motions of the atomic structure, hence the huge D-peak proves that the individual graphene lattice is very disrupted in turbostratic graphite. It is profoundly disordered on the nanoscale. It can no more be restored to a 2-D graphene material. Researchers have lamented the slow development of the field of research into the very promising area of turbostratic graphene due to the difficulty of obtaining the material.[8, 11] Turbostratic graphene was only produced in trace amounts (by weight) by CVD or epitaxial growth. And even growth under these carefully controlled growth conditions, it does not assure that the material will be turbostratic. One group that attempted a thickness of 10-layer turbostratic graphene using CVD on nickel foil obtained varying results, sometimes AB-stacked, sometimes turbostratic, and sometimes a mixture of the two.[9] Even this recently developed process to multilayer growth of turbostratic graphene has been difficult to make reliable.

Number of layers does not define 2-D character

Several authors have reported that for AB-stacked graphene, the 2-D properties of single-layer graphene (SLG) or few-layer graphene (FLG) gradually transition to 3-D material with the Raman spectra evolving into that characteristic of HOPG at about 10 layers.[3, 13] However, this rule of thumb does not apply to turbostratic graphene because the individual layers are weakly coupled, so they retain the 2-D character independent of the number of stacked layers.[7, 9] The 2D peak retains its narrow Lorentzian lineshape, and no additional states are introduced to the Dirac cone at the K-point. Hence the Raman scattering for the 2D peak remains a single peak that is doubly resonance enhanced, giving rise to its strong enhancement. And it remains a zero band gap semiconductor. In contrast, when two layers are AB-stacked, the strong coupling creates additional states with a parabolic shape around the K-point, which allows for more transitions. The 2D peak becomes a sum of four Lorentizians, two strong and two weak, and it substantially broadens while losing its Lorentzian line shape. Several authors have studied rotationally misoriented graphene, some by the method of folding a single sheet, which guarantees misalignment. As a result of the poor overlap of the 2p atomic orbitals, the two sheets retain their SLG characteristics.[7, 9, 11]

The presence or absence of certain relative weak Raman combination bands are positive indicators for the occurrence of turbostratic graphene: "Combination Raman modes of as-grown graphene within the frequency range of 1650 cm^{-1} to 2300 cm^{-1}, along with features of the Raman 2D mode, were employed as signatures of turbostratic graphene." There is a "combination of in-plane transverse acoustic (iTA) and the longitudinal optic (LO), iTA and longitudinal acoustic (LA) and LO + LA modes. Here, we designate the iTALO− mode as TS_1 and the iTOLA/LOLA modes as TS_2."[11]

Using TS_1 and TS_2 as positive indicators

We will use the designations of TS_1 and TS_2 to indicate these two features that are Raman active only for SLG and turbostratic graphene. TS_1 is a single Lorentzian that occurs in the vicinity of 1880 cm^{-1} and TS_2 consists of two closely space Lorentzians that occurs in the vicinity of 2030 cm^{-1}; however, it must be kept in mind that these lines exhibit dispersion, like many Raman features in graphene. The excitation wavelength must always be noted, and dispersion corrections applied when comparing the peak frequencies.

The silent M band

In addition, the "M" band occurs about 1750 cm^{-1} but this combination band becomes silent for turbostratic graphene. Hence the presence of the M band is a negative indicator for turbostratic graphene, and a positive indicator for AB-stacked graphene as well as HOPG.

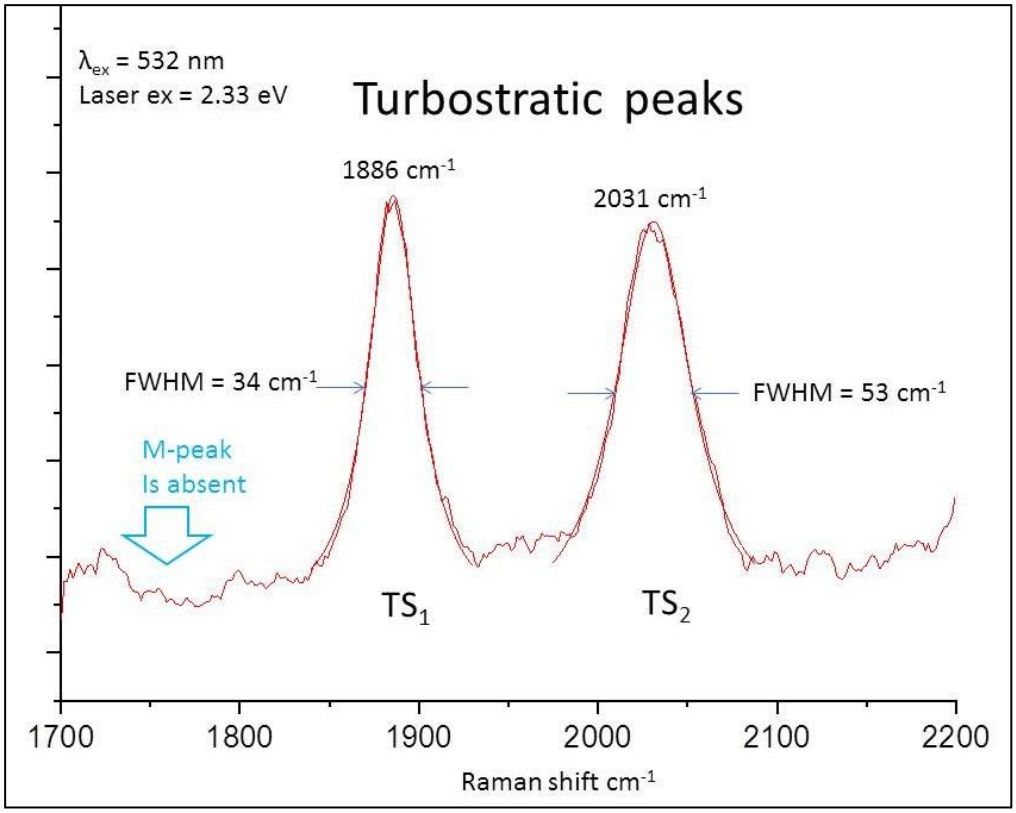

Supplementary Fig. 2. Turbostratic peaks in the Raman spectrum of CB-FG. $I_{G/TS1}$ ~30. Lorentzian fit is shown as a superimposed smooth line. The R-squared is 0.994 for TS_1 and 0.99 for TS_2. These excellent fits indicate the high quality of the FG and the unmistakable presence of these Raman lines are attributable to turbostratic graphene.

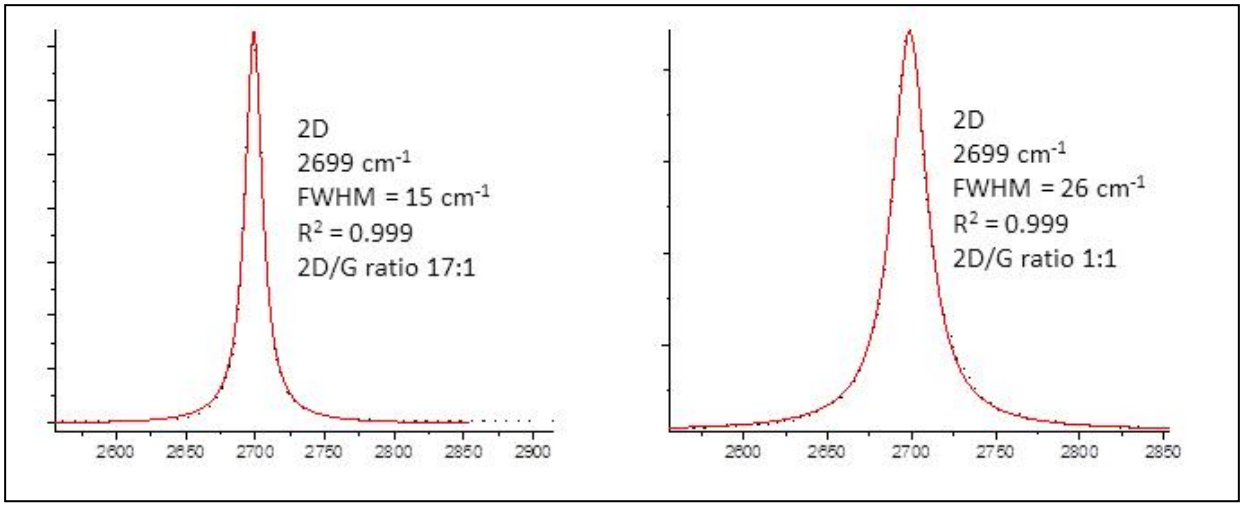

Supplementary Fig. 3. 2D peak in the Raman spectrum of CB-FG. Left: best point in CB-FG, right: representative point in CB-FG. Both peaks exhibit nearly a perfect Lorentzian line shape. The black dots are the theoretical line shape. The R^2 for the correlation is 0.999 for both peaks. This is indicative of a fully conical Dirac cone at the K-point. The exceptionally large $I_{2D/G}$ is also indicative of multilayer turbostratic graphene, as several researchers point to an increasing $I_{2D/G}$.[7, 11]

The narrow, single Lorentzian 2D peak can occur only for either SLG or turbostratic graphene whereby the adjacent layers are decoupled and do not give rise to additional electronic states. This in turn means that it remains perfectly 2-dimensional, even though there are many layers of graphene stacked. For the best example on the left of Fig. 3, the Lorentzian full-width-at-half-maximum (FWHM) has actually become narrower than for the perfect SLG. This narrowing is a unique feature of rotationally misaligned graphene that is stacked and only occurs for turbostratic graphene, as describe below relative to other reports. We have observed 2D peaks as narrow as 15 cm^{-1}, which occurs only for multiple layers of turbostratic graphene. The much broader band is for a Bernal bilayer, which is a sum of four peaks and is clearly non-Lorentzian.

Comparison of the Raman spectrum of CB-FG to those in reported turbostratic graphene

Supplementary Table 1: Comparison of 2D, TS_1 and TS_2 peak with previous studies. The peak position from previous studies that used 514 nm excitation laser are corrected to match the 532 nm excitation laser in this study.

	2D		TS_1		TS_2	
	Position	FWHM	Position	FWHM	Position	FWHM
Niilisk *et al.*[9]	2697	36	1886	34	2030	54
Garlow *et al.*[11]	2702	27	1884	38	2031	51
CB-FG	2699	15-26	1886	34	2031	53

Comparing CB-FG spectra with data from two different references, the locations and FWHM of the two TS (turbostratic) peaks are essentially identical in both cases. The location of the 2D peak is also the same, with the CB-FG Lorentzian matching the narrower FWHM in that from Garlow *et al.* We have observed 2D peaks as narrow as 15 cm^{-1}, which occurs only for multiple layers of turbostratic graphene. Comparing to Niilisk *et al.*, which has up to 6 layers of turbostratic graphene, again there is a near identical match with the TS_1 and TS_2 peaks both in frequency and width. And for both references and our CB-FG, the M-peak which is characteristic of both AB-stacked graphene and HOPG, is absent. Therefore, there are several precise and redundant spectral feature alignments between the turbostratic CB-FG Raman data and two references that have obtained Raman spectra from proven turbostratic graphene. In addition, the narrowing of the 2D Lorentzian FWHM is further support of the turbostratic stacking as a 2-D material.

The very small D-band

Interestingly, not all edges behave as defects; hence they will not always display a D-band. For the zigzag edge, the phonon that gives rise to the D-band remains silent. Since the zigzag edge is the most probable edge for freely growing graphene then that phonon for the edges can remain silent, thus the D-band remains very small as observed. This was experimentally verified when Yan et al. did a thorough Raman map of their large hexagonal single-crystal graphene and the D-band remained very small at the edges.[19]

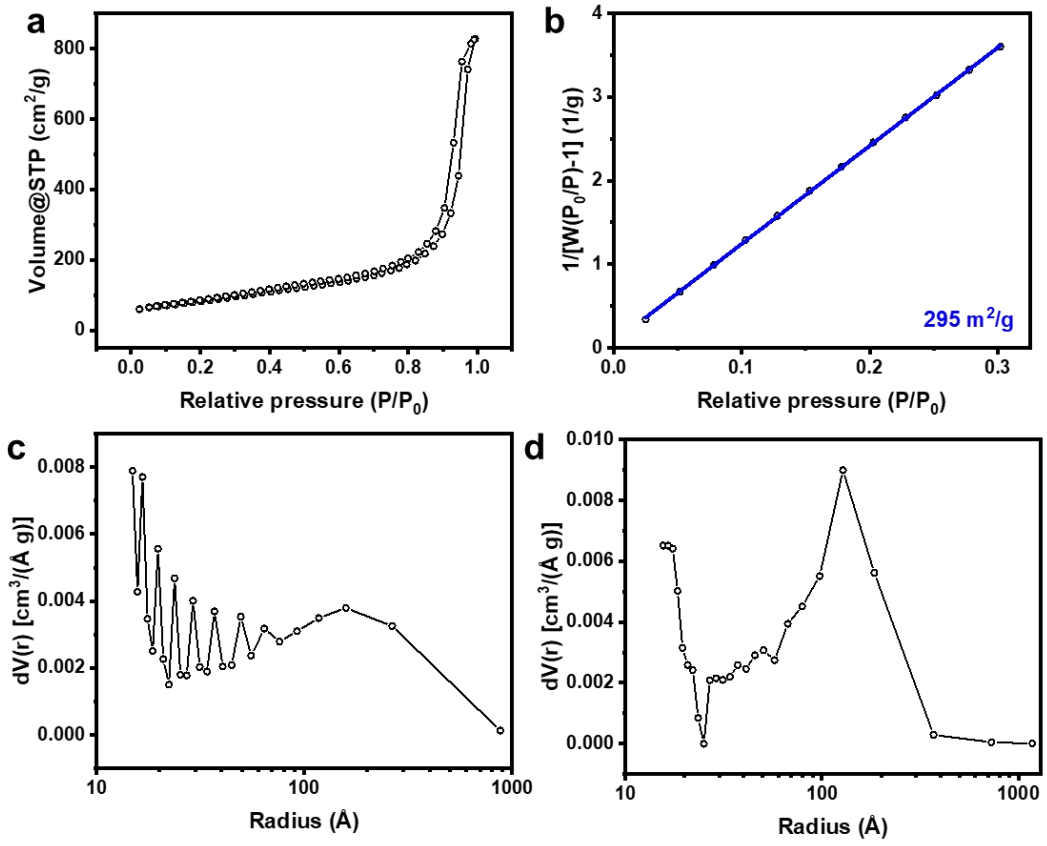

Supplementary Fig. 4. **BET surface area analysis of CB-FG.** a. Isotherm. b. BET surface area fitting. c-d. Absorption and desorption pore size distribution.

Supplementary Table 2: FJH parameters for various materials in Fig. 1. Duration is the switch opening time, not the real flash duration. Blue colors in the voltage row signify pre-treatment without a flash, red colors signify an actual flash during the FG synthesis. The pre-treatment is to partially char the material to reduce the volatile material and increase the conductivity. The charring process affords only amorphous material by Raman analysis. This pre-treatment is crucial for starting materials with low carbon content. This pre-charring can be obviated with a beneficiation material wherein there is a pre-heat cycle since industrial heating is less expensive than using electricity when heating below certain temperatures. And we also list a beneficiation material, rubber tire-derived carbon black, where the volatiles were industrially removed, leaving a carbon residue (see the rubber materials section).

Starting material	**Weight (mg)**	**Tube (mm)**	**Capacitance (mF)**	**Resistance (Ω)**	**Voltage** **Pretreat** **Flash**	**Duration (ms)**	**Result material**
Carbon black (Black Pearls 2000, Cabot)	30	4	60	1.5	35 V x 5 110 V	500 50	CB-FG (highest $I_{2D/G}$)
	120	8	60	1	60 V x 5 220 V	500 500	CB-FG (plastic compounding)
	1200	15	220	1.5	100 V x 5 250 V	500 500	CB-FG (1.1 g batch)
Used coffee grounds/ CB	1000	10	220	1000-3000	150 V x 3	10000	Charred coffee grounds

(5%) (Starbucks and Folgers)							
Charred coffee grounds	50	4	60	5-10	40 V x 5 130 V	50	C-FG
Anthracitic coal (Fisher Scientific S98806)	80	4	60	2000-3000	150 V	10000	Anthracite-derived FG
Calcine coke (Oxbow Calcining International, CPC 1400)	80	4	60	0.8	80 V x 5 175 V	100 500	Calcined coke-derived FG

Flash Graphene Morphology

Most organic compounds will graphitize when annealed at elevated temperature. During the graphitization process, an organic material is heated, increasing carbon content via pyrolysis. During pyrolysis, the carbon forms sp^2-hybridized covalent bonds with neighboring carbon atoms and crystallizes into layered domains of graphite. Non-carbon elements volatilize at the extreme temperatures. However, the structure of graphitized material largely depends upon the method of preparation as well as the starting material. Some of the earliest work to critically comment on the various morphologies of carbon graphitization was that of Rosalind Franklin,[20]

which studied morphologies purely by means of x-ray diffraction and density measurements. It was noted that after heating several non-graphitic carbons to temperature between 1700 and 3000 °C, layers of sp^2-hybridized carbon would orient into relatively dense crystalline graphite. These were termed *graphitizing carbons*. Other carbon starting materials would form porous graphite-like layers in parallel groups when annealed, without extended stacking along the c-axis. These were termed as *non-graphitizing carbons.*

With the advent of atomic resolution microscopy techniques, the structure of *graphitizing* and *non-graphitizing carbons* could be visualized to further reveal their morphologies. High resolution TEM images have shown that non-graphitizing carbons, such as polyvinylidene chloride and carbon black, may form closed carbon nanoparticles which are fullerene-like in structure,[21] and resemble the simulated structure of flash graphene reported in Figure 3d of the manuscript. These particles are characterized by lattice fringes along all sides, which suggest a 3-D fullerene-like structure. Work by Iijima reveals that graphitized carbon black can form fullerene-like polyhedra of carbon which are single to few layers in thickness.[22] These were named graphene polyhedra. These structures are characterized by angles of ~ 120 ± 20^o along the edge of the graphene polyhedra and suggest the presence of some 5-7 member rings required for bending. Later, Dresselhaus et al. observed the real-time graphitization of amorphous carbon via Joule heating in a transmission electron microscope.[23] Of particular interest, formation of graphene polyhedra particles are observed upon Joule heating, with the thickness of the graphitic shell increasing with annealing time. Other work by Wang et al. demonstrated that the electro-graphitization and exfoliation of carbon nanofibers can be afford graphene.[24] However, Raman analysis reveals a relatively poor quality of graphene by electrographitization.

In this work, various morphologies of graphene can be found ranging from sheets of graphene to graphene polyhedra, as shown in Figure 1 of the manuscript. These morphologies largely depend upon the carbon starting material which reflects whether the starting material is a *graphitizing* or *non-graphitizing* carbon; however, unique to the FG process, heating and cooling occurs over the timescale of milliseconds. Fast heating and cooling rates prevent the stacking of graphene layers to form graphite, and it also prevents the rotational registration of graphene layers thus resulting in turbostratic graphene. This gives rise to the exceptional graphene quality observed spectroscopically. All carbon sources that were flashed exhibited at least some morphologies which are of the graphene polyhedral type. Figure 1 from the manuscript shows that flash graphene in this work can have a similar polyhedron structure to that mentioned in literature with many edge angles ranging from 109 – 130°. The polyhedra are commonly composed of <5 layers which constitutes classification as FLG. However, some carbon starting materials will also form sheets when Joule heated. A summary of our flash graphene morphologies can be found in Supplementary Table S2. Though not optimized for all the starting materials, materials such as anthracite coal, coffee, biochar, calcined coke, and pine form graphene sheets. This is consistent with the finding that that all of our FG carbon sources which form graphene sheets have formerly been classified as *graphitizing carbon* in literature reports (Supplementary Table S2). Hence, the resultant morphology of FG largely depends on the starting carbon source. Materials classified as *graphitizing carbons,* which will readily pyrolyze into graphite when thermally annealed, generally result in the partial formation of graphene sheets when flashed. Materials classified as *graphitizing* and *non-graphitizing carbons* all result in the formation of graphene polyhedra during the flashing process. This suggests that the rapid heating and cooling rates associated with FJH effectively retards further crystallization of the

graphene polyhedra into graphitic domains, thereby giving rise to unique structures not typically found in furnace-heated graphitized material which undergo a relatively slow heating and cooling. FG structures are composed of ultra-high purity, low defect material which give rise to exceptional Raman signatures, such as a $I_{2D/G}$ ratio of up to 17.

Supplementary Table 3. Table reporting the presence of graphene polyhedra or graphene sheets when forming flash graphene from each carbon source. Comparison to literature shows that *graphitizing carbons* (which are known to form graphite upon pyrolysis) result in formation of graphene sheets. All flashed materials exhibit some graphene polyhedral.

Carbon Source	**Graphene polyhedra**	**Graphene sheets**	**Pyrolysis morphology in references**
Carbon black	Yes	No	Pyrolysis forms graphene polyhedra[20, 25]
Calcined petroleum coke	Yes	No	Pyrolysis forms crystalline graphite domains[20]
Coffee grounds	Some from CB conductive dopant	Yes	Pyrolysis of cellulose and lignin forms crystalline graphite domains[26, 27]
Anthracite coal	Some from CB dopant	Yes	Pyrolysis forms crystalline graphite domains[20]

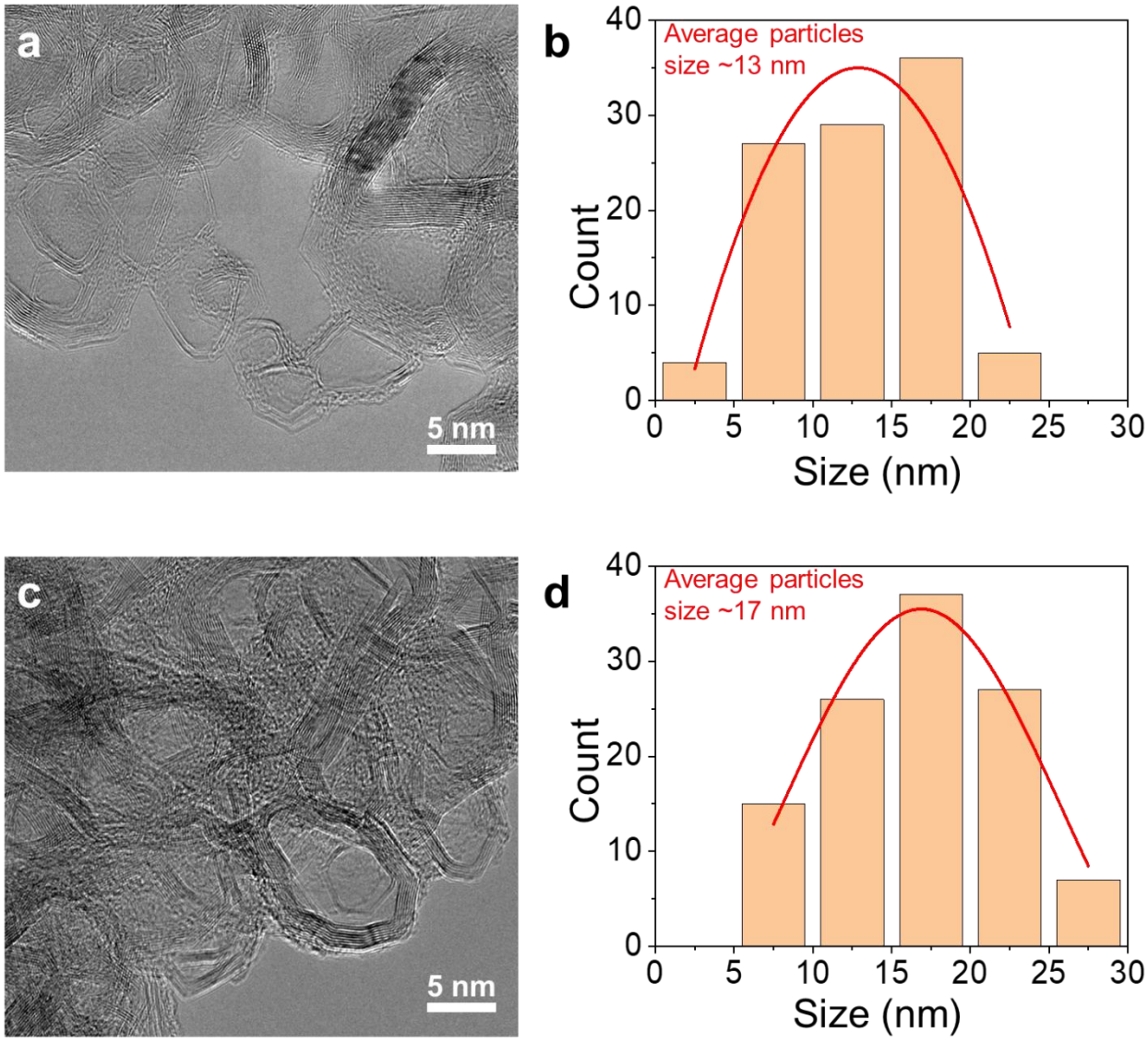

Supplementary Fig. 5. **Size distribution of CB-FG and CPC-FG.** a. HR-TEM image of CB-FG. b. Histogram for size distribution of CB-FG. c. HR-TEM image of CPC-FG. d. Histogram for size distribution of CPC-FG.

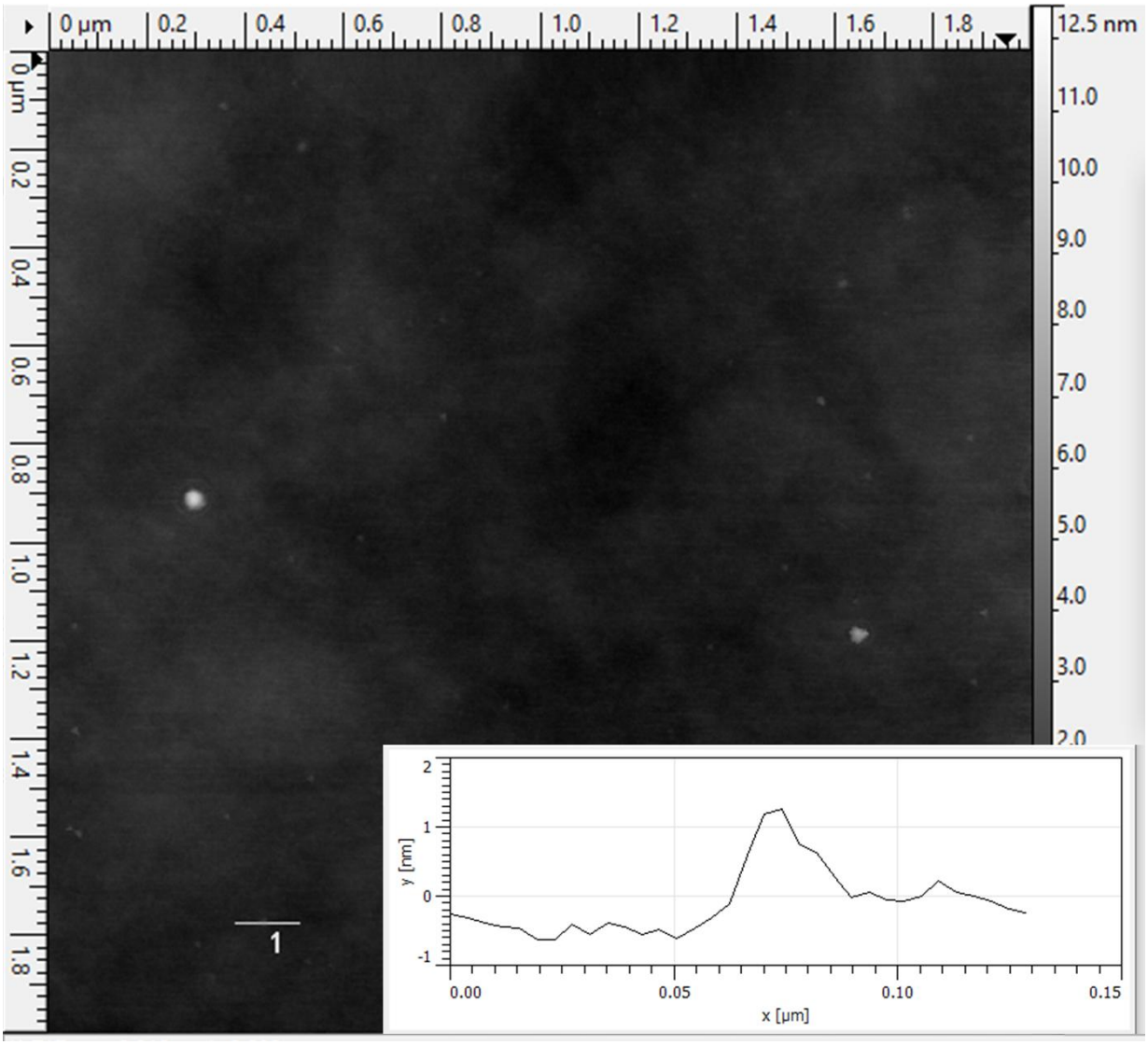

Supplementary Fig. 6. **AFM characterization of carbon black-derived FG.** CB-FG is dispersed in *N*-methyl-2-pyrrolidone (NMP) solution and deposited onto a silicone substrate. The individual CB-FG particles as seen from Supplementary Fig. 5 lay on the surface with height of ~ 1.2 nm that result from FLG.

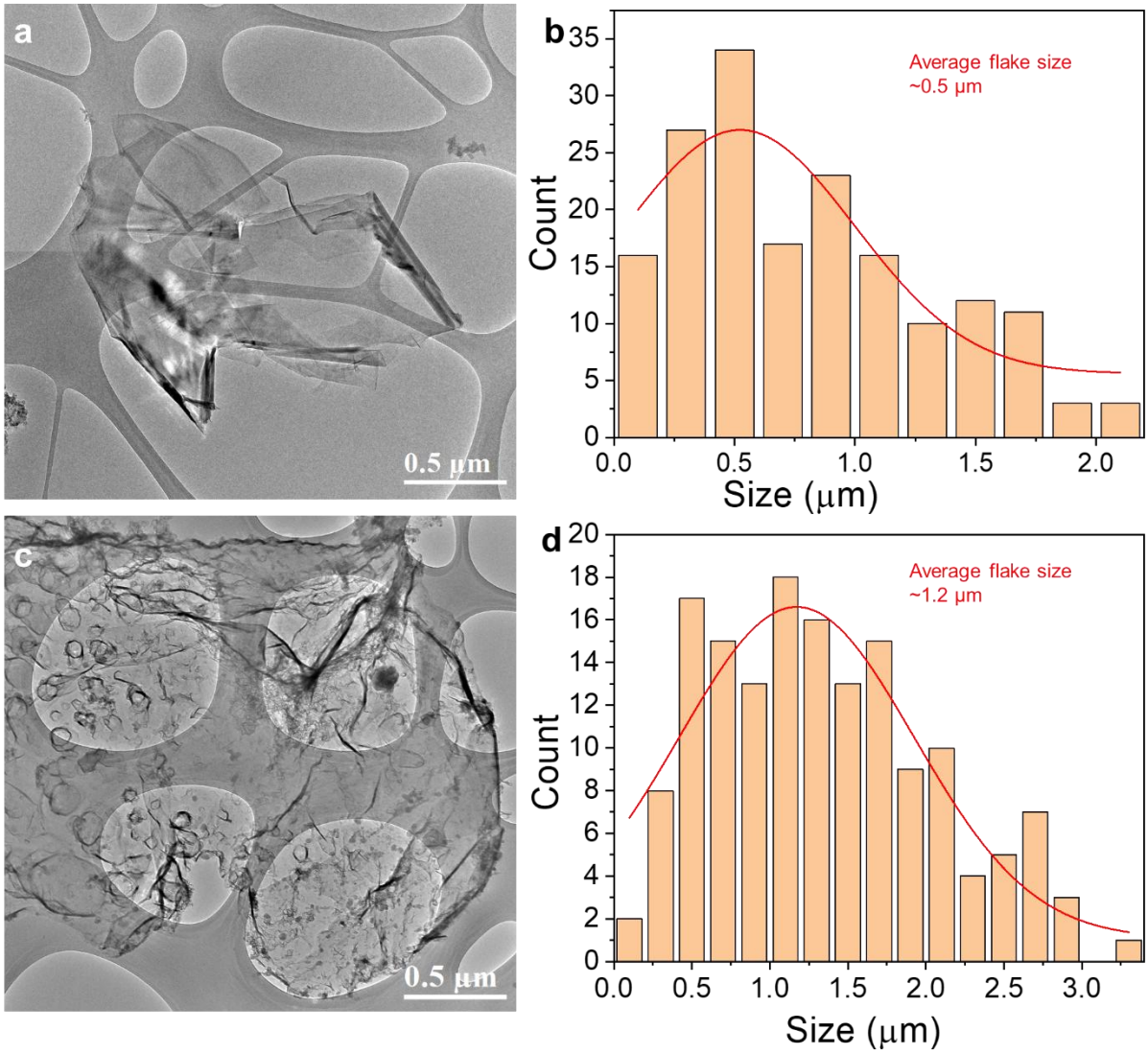

Supplementary Fig. 7. **Size distribution of anthracite- and coffee-derived FG.** a. HR-TEM image of A-FG. b. Histogram for size distribution of A-FG. c. HR-TEM image of C-FG. d. Histogram for size distribution of C-FG.

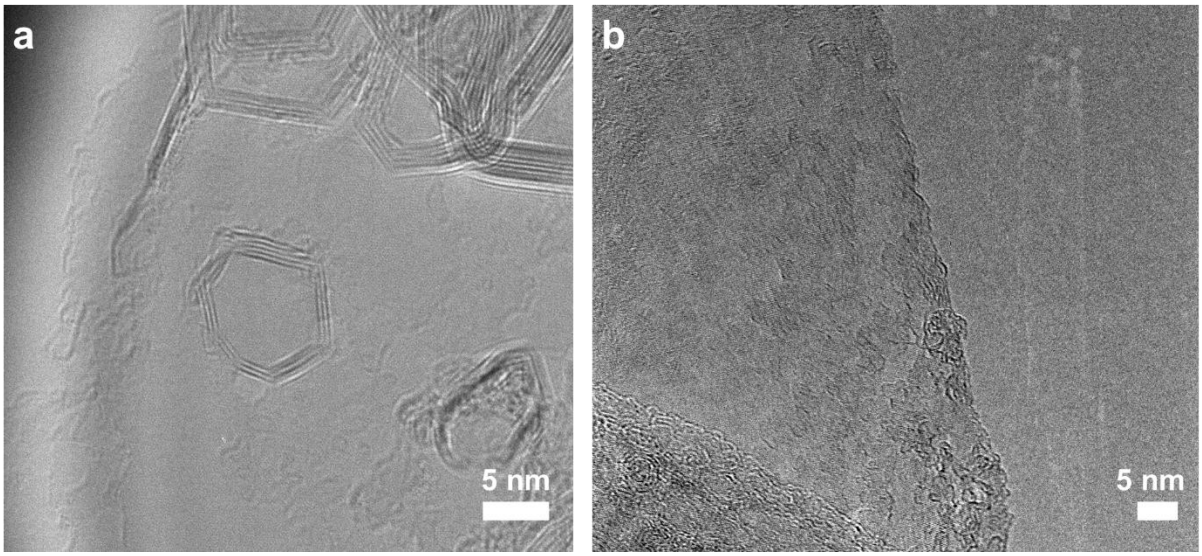

Supplementary Fig. 8. TEM images of single layer of graphene from (a) C-FG and (b) A-FG. The CB-FG has some polyhedral graphene that could also come from the CB dopant used to increase the conductivity for FJH.

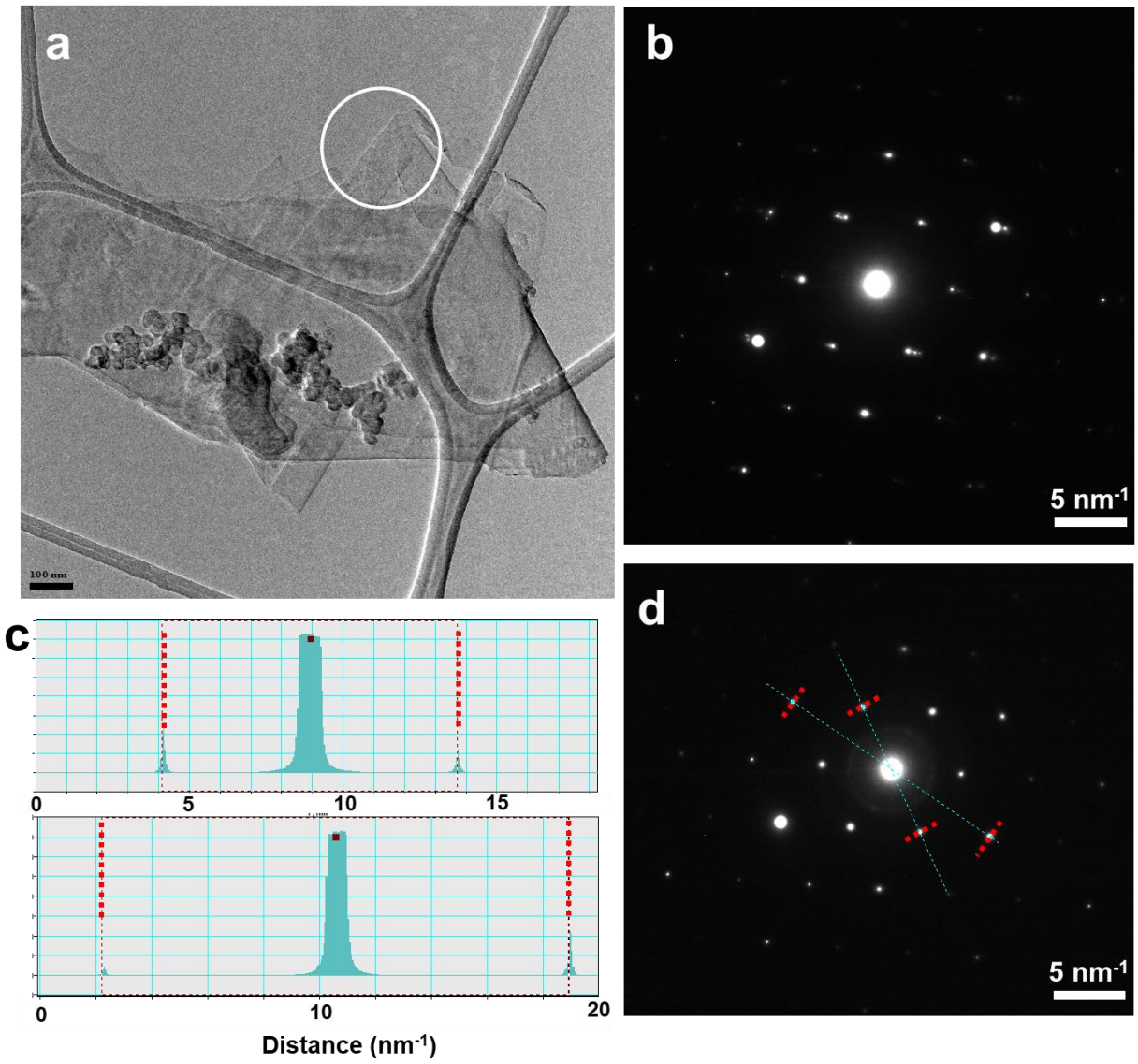

Supplementary Fig. 9. **SAED of anthracite-derived FG**. a. TEM image of a A-FG flake and the position for SAED. b. SAED of the few-layer graphene position that shows misalignment between layers. c-d. SAED of SLG that correlates with SLG in previous studies.[28, 29]

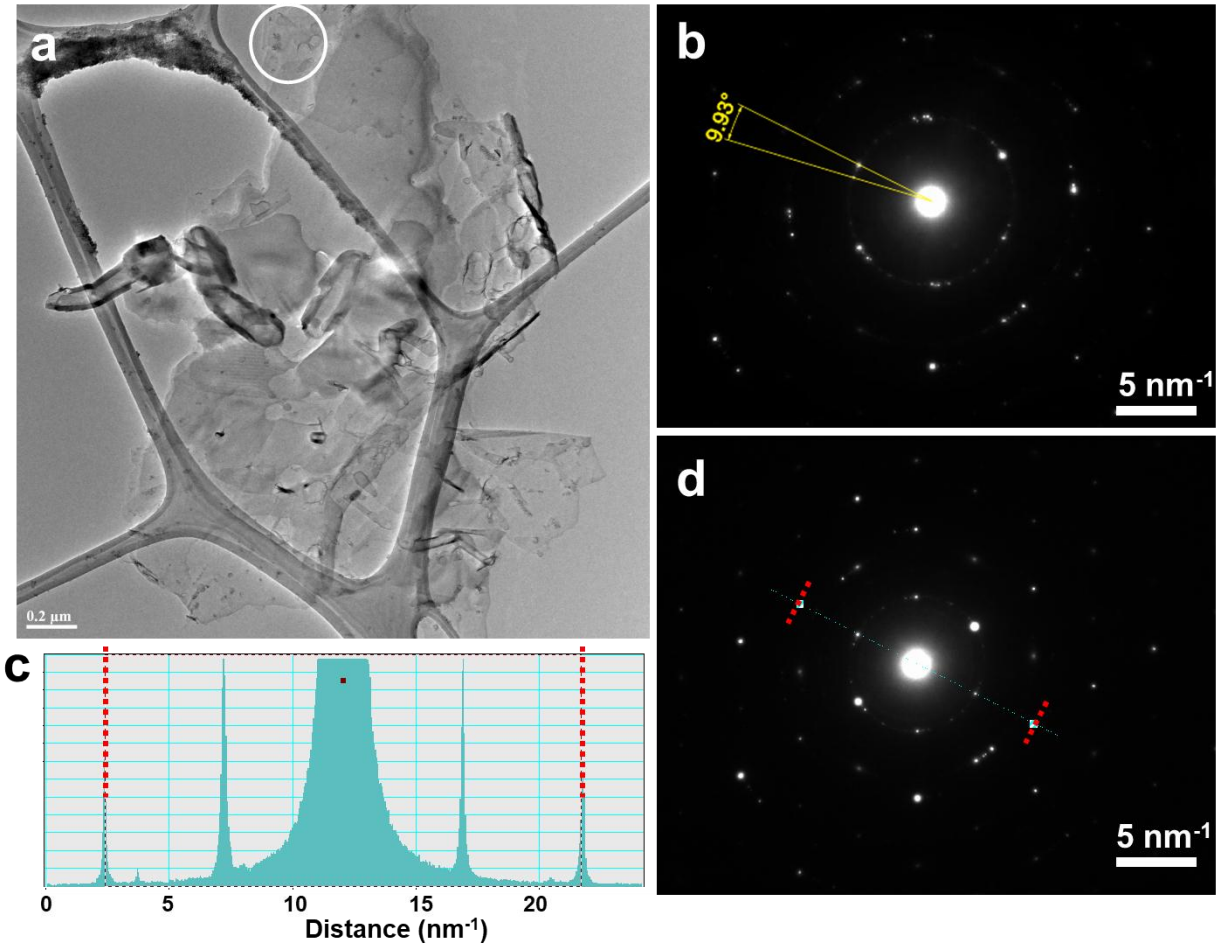

Supplementary Fig. 10. **SAED of coffee-derived FG**. a. TEM image of a C-FG flake and the position for SAED. b. SAED of the few-layer graphene position that show misalignment between layers. c-d. SAED of a SLG that correlates with SLG in previous studies.[28, 29]

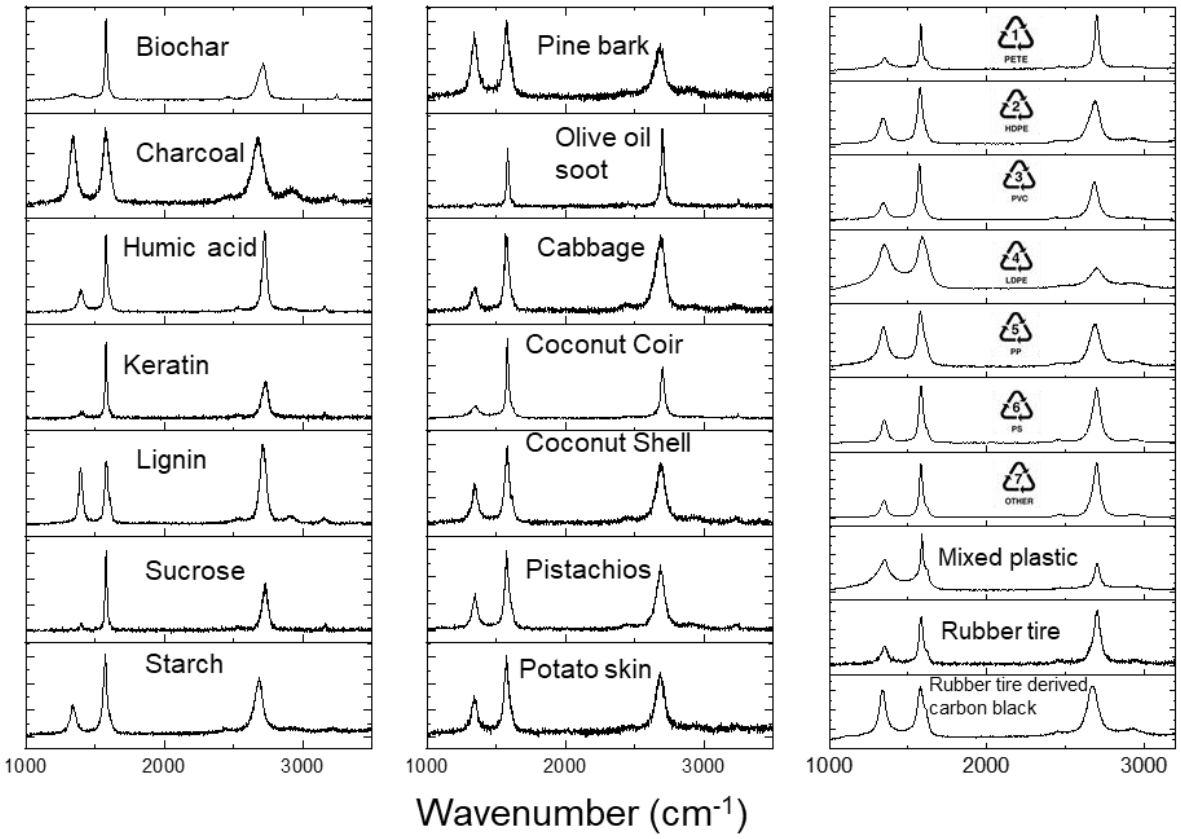

Supplementary Fig. 11. Representative Raman spectra of FG derived from other carbon sources. None of these have been optimized for FJH conditions to maximize the graphene quality. Biochar was sufficiently conductive; it needed no additive. All other non-plastic samples had 5 to 10 wt% CB added to increase their conductivities. All plastic samples had 5 wt% CB added to increase their conductivities. Or 2 to 5 wt% of FG from a previous run can be used to substitute the CB as the conductive additive, but those spectra are not shown here. #7 plastic, "OTHER", is polyacrylonitrile (PAN). Mixed plastic was made from the following wt% of polymers: HDPE 40%, PETE 40%, PP 10%, PVC 10%.

Supplementary Table 4. Precursor sources for Supplementary Fig. 11. Pine bark, olive oil soot, cabbage, keratin from human hair, coconut, pistachio shells, potato skins, PETE, HDPE, PVC, LDPE, PP, and PS were collected as waste products, so they were not purchased.

Biochar	Neroval LLC, from mixed Tennessee hardwoods, commercially prepared at 1100°C
Charcoal	Sigma CAS: 7440-44-0
Humic acid	Sigma CAS: 1415-93-6
Lignin	Sigma CAS: 8068-05-1
Sucrose	Sigma CAS: 57-50-1
Starch	Argo gluten free
PAN	Sigma CAS: 25014-41-9
Rubber tire-derived carbon black	Ergon Asphalt and Emulsion Inc.

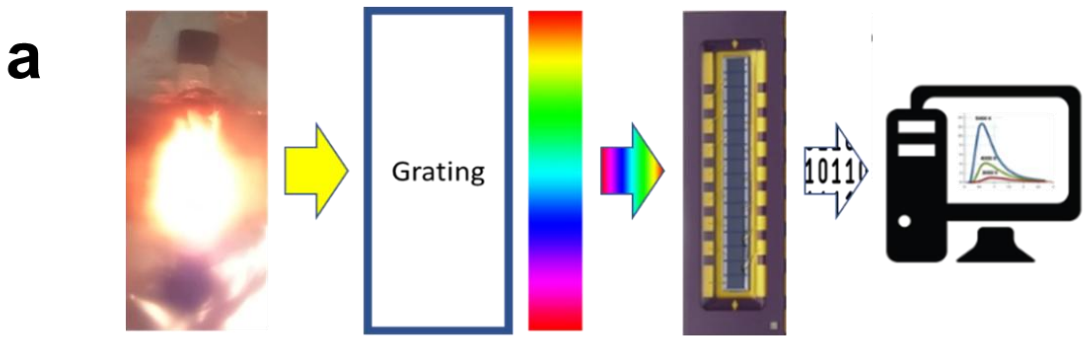
a
Grating
1011

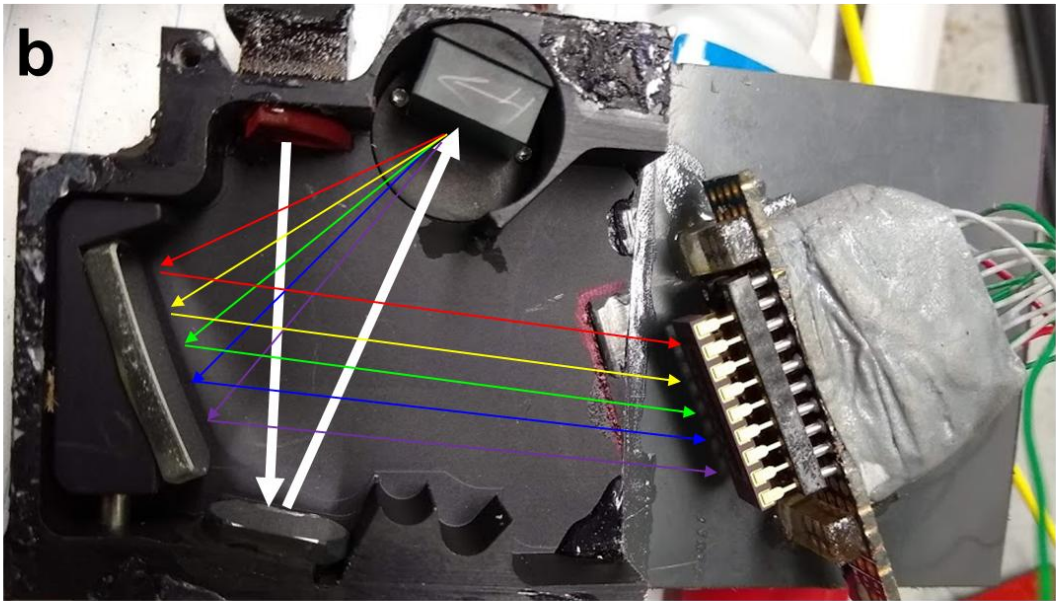
b

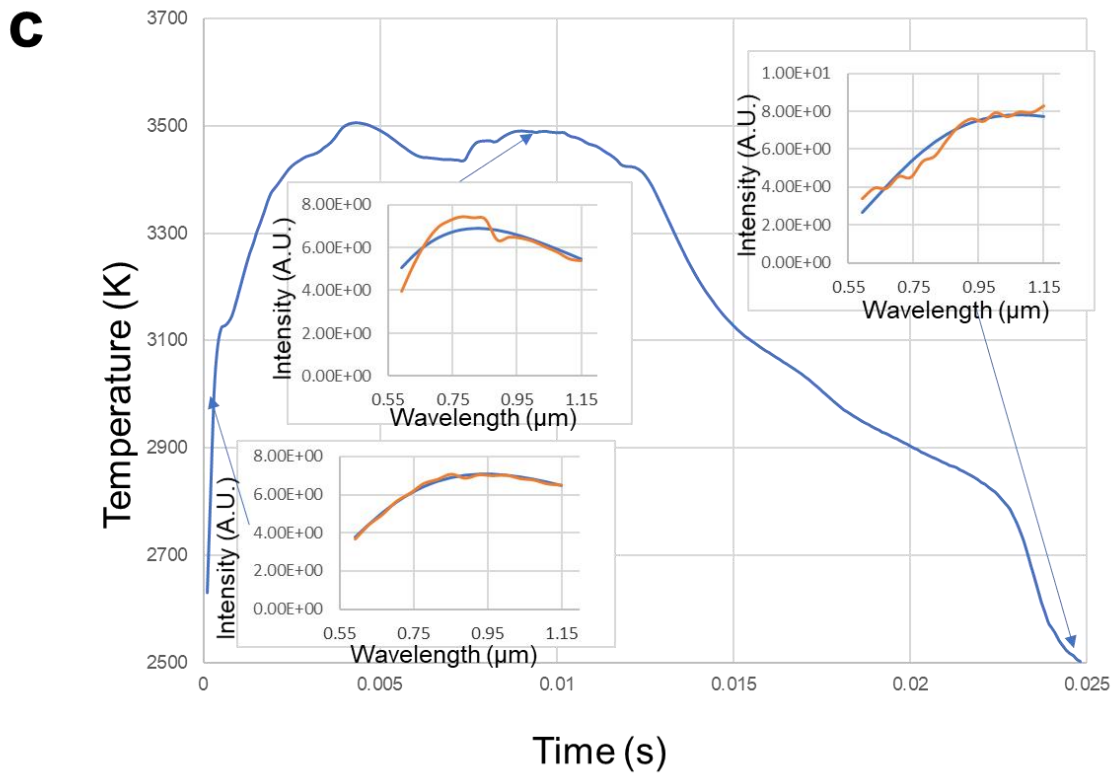
c
Temperature (K)
Time (s)
Intensity (A.U.)
Wavelength (μm)

Supplementary Fig. 12. Ultrafast temperature measurement. a. Schematic of the home-built temperature measurement set up. b. Black body radiation from the sample is collected by an optical fiber through a customized grating black box. The spectrum of the radiation populates a 16 pixels photodiode arrays (Hamamatsu S4111-16R) at 600 nm to 1100 nm. Light paths are illustrated. The reversed bias voltages (9 V) from the photodiode arrays are collected by the National Instrument multifunction I/O device PCIe-6320. c. Black body radiation fitting. The temperature from each point of the temperature *vs* time graph is determined by the black body radiation fitting of the spectrum from 0.6-1.1 μm emission. Inset is spectrum fitting for 3000 K, 3500 K and 2500 K.

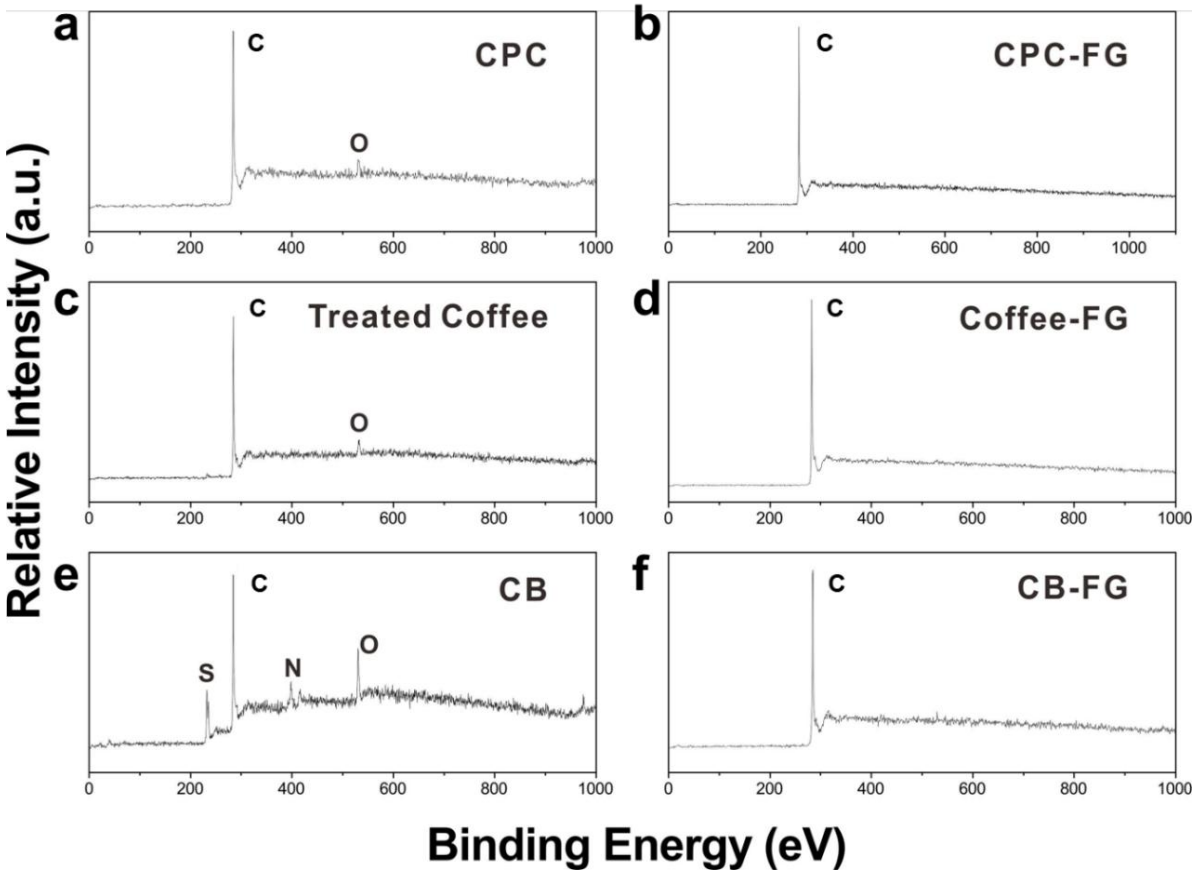

Supplementary Fig. 13. XPS of calcined petroleum coke, pre-treated (see main text) coffee grounds and carbon black before and after the FJH process. Significant reduction in contaminants is seen with FG from carbon black.

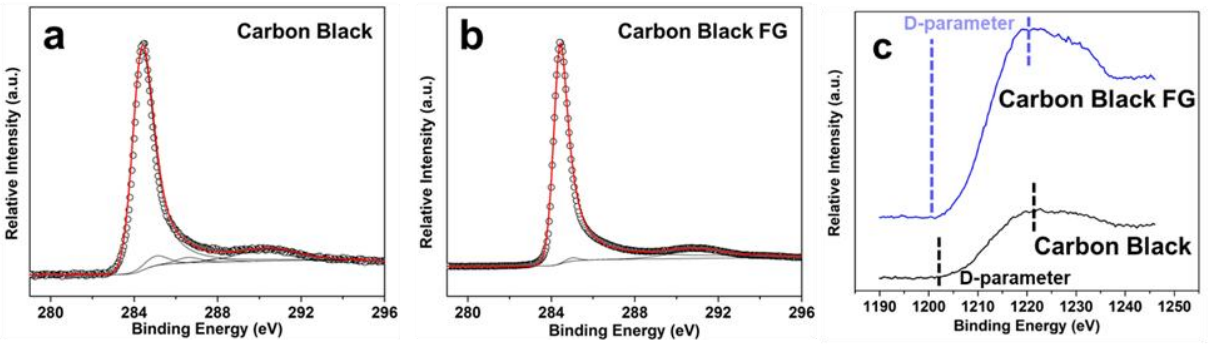

d	C=C (sp2)	C-C (sp3)	C-O/C-O-C	O-C=O/C=O
CB (%)	90.9	4.7	2.8	1.6
CB-FG (%)	98.6	1.4	0	0

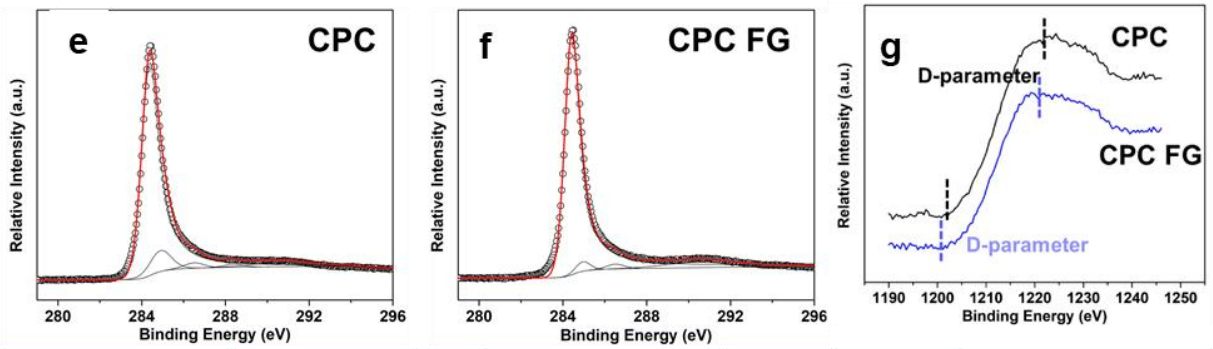

h	C=C (sp2)	C-C (sp3)	C-O/C-O-C	O-C=O/C=O
CPC (%)	84.7	11.1	2.6	1.5
CPC-FG (%)	93.9	3.7	2.4	0

Supplementary Fig. 14. **High resolution XPS of the C 1s spectrum from CB-FG and CPC-FG**. a. CB. b. CB-FG. c. High resolution XPS of C KLL spectrum of CB and CB-FG. The D-parameter measures the energy separation between maxima and minima in differentiated C KLL spectra. In diamond and graphene, the values are 13 eV and 21 eV, respectively. The larger values infer a higher sp^2/sp^3 ratio.[30] For the CB and CB-FG, the values are 20.5 eV and 20.9 eV, respectively. Thus, after the FJH process, the sp^2/sp^3 ratio increases in going from CB to CB-FG.

d. Relative distribution of deconvoluted C 1s peak high resolution spectrum of CB and CB-FG. Relative distribution of sp^2-carbon (C=C) increases from 90.9% to 98.6% and the sp^3-carbon (C-C) decreases from 4.7 % to 1.4 %. Thus, the sp^2/sp^3 ratio increases after the FJH process, corroberating with the very high 2D/G ratio in the Raman spectra of CB-FG. d. Relative distribution of deconvoluted C 1s peak high resolution spectrum of CPC and CPC-FG. The sp^2/sp^3 ratio increases from 7.6 to 25.2 after the FJH process, corroborating with the very high 2D/G ratio in the Raman spectra of the CPC-FG.

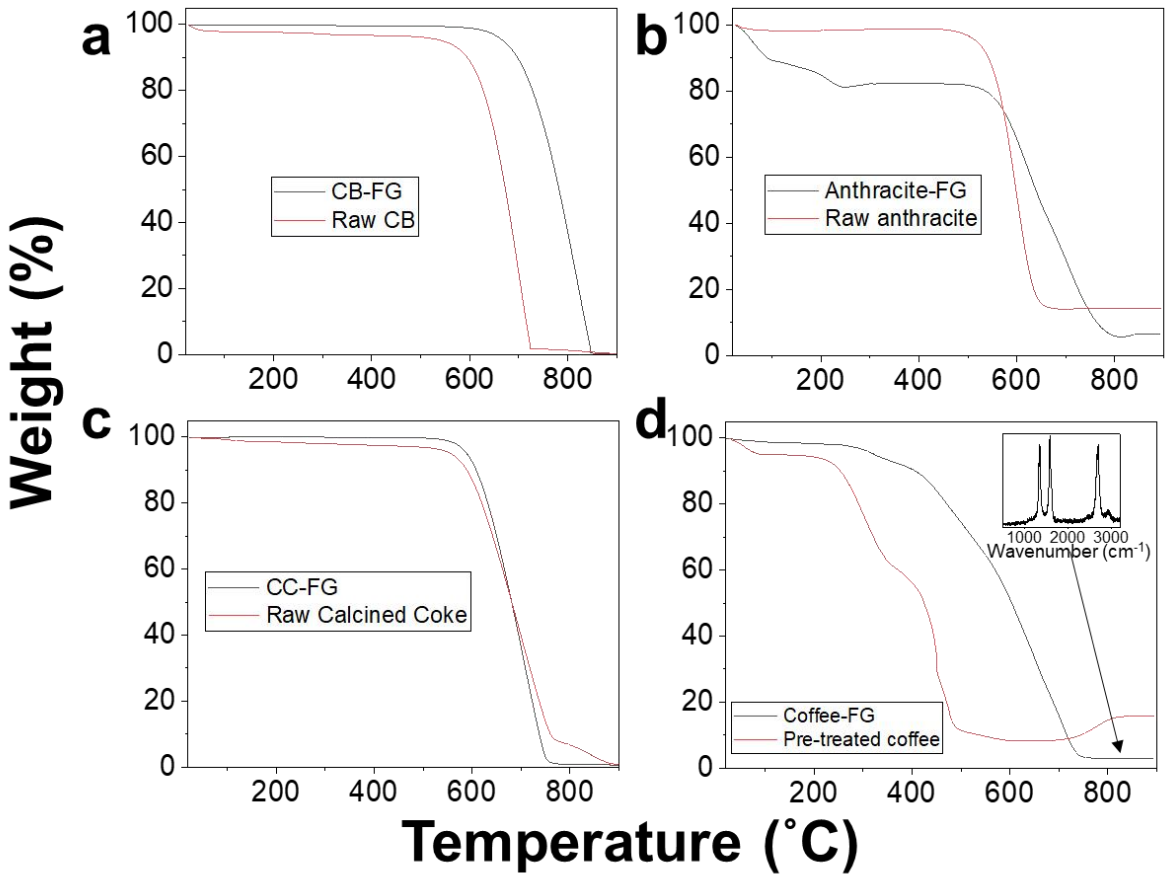

Supplementary Fig. 15. TGA in air of: a. Raw CB (Black Pearls 2000, Cabot) and CB-FG. b. Raw anthracite coal and anthracite-FG. c. Raw calcined coke and CC-FG. d. Pre-treated coffee

and coffee-FG. With carbon black, anthracite coal and coffee, there is significant decrease in the final weight between the precursor material and the derived FG. XPS of the TGA residue shows that the TGA-residue from anthracite-FG contains of C (15%), O 62 %, Si (11%) and Al (12.6%); and residue from coffee-FG contains of C (65%), O (25%), S (2.9%) and P (2%). Furthermore, the TGA-residue from coffee-FG was analyzed by Raman spectroscopy (inset in d) to show that it is significantly graphene.

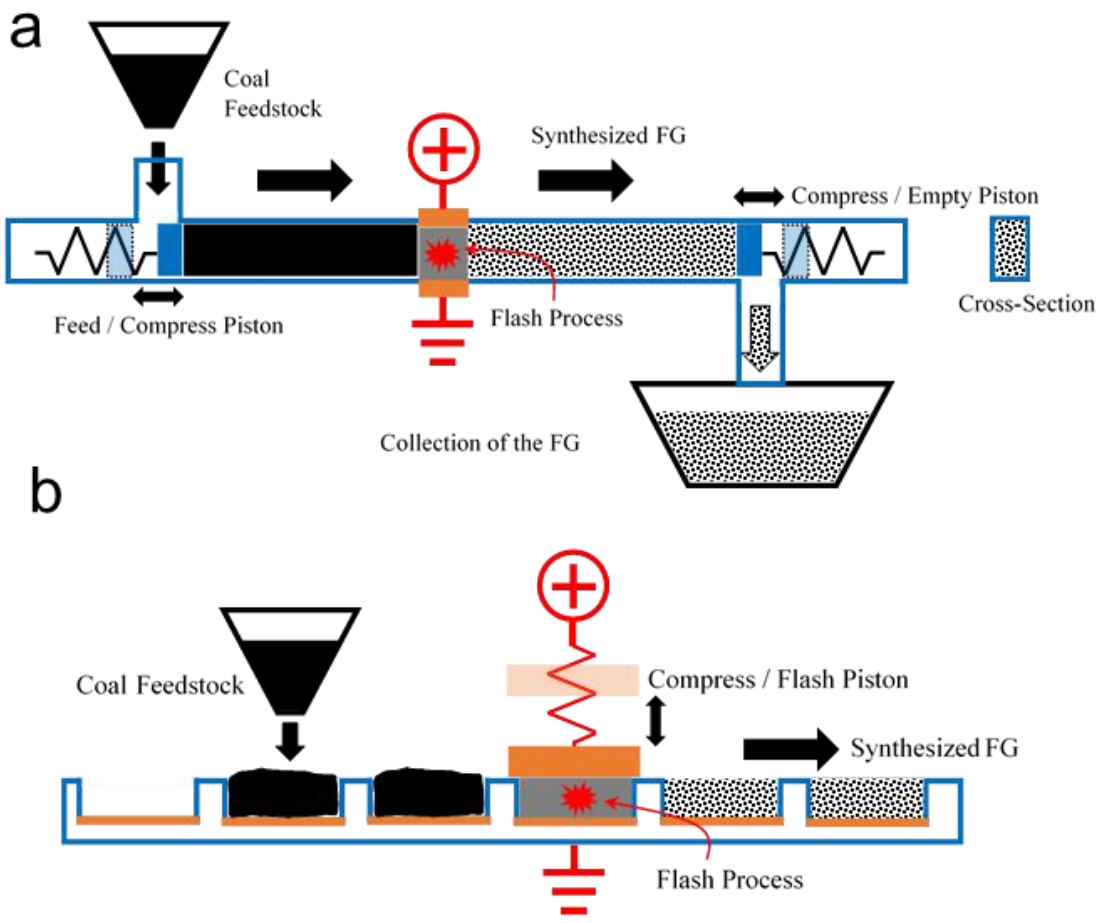

Supplementary Fig. 16. Possible reactors for automation of the FG process, for example with a coal source. a. Continuous piston FG process. Unlike the laboratory setup, the function of the compression pistons and the electrodes is carried out by separate components. Suitable electrodes are copper, stainless steel, graphite or tungsten electrodes that are attached to the quartz but have vent holes to enable escape of the hot process gases during the FJH process. The compression pistons can be made of a dielectric material, possibly quartz or ceramic, to prevent shorting to the piston's ground. In this continuous process, carbon feedstock is fed through a reservoir into the process tube (aided by a shaker) while the compression piston is retracted to the left. After the carbon powder is dispensed in the tube, the Feed Compress Piston moves with enough stroke to displace the converted carbon from underneath the electrodes (JH region) while at the same time the Empty Compress Piston retracts to the right to allow FG to be emptied into a collection bin (aided by a shaker or a vacuum suction). After the strike is over, the Empty Piston pushes in to block the tube while the Feed Piston applies predetermined pressure to the coal until the FJH process is done. The piston cycles need to match the throughput of the continuous process. The flow of carbon/FG material is in an enclosed environment that makes the operation safe. b. Continuous Belt FG Process. In this reaction, the coal feedstock is fed through a reservoir into the quartz or ceramic boat, having a metallic bottom electrode that is grounded electrically, and is part of a continuous belt.

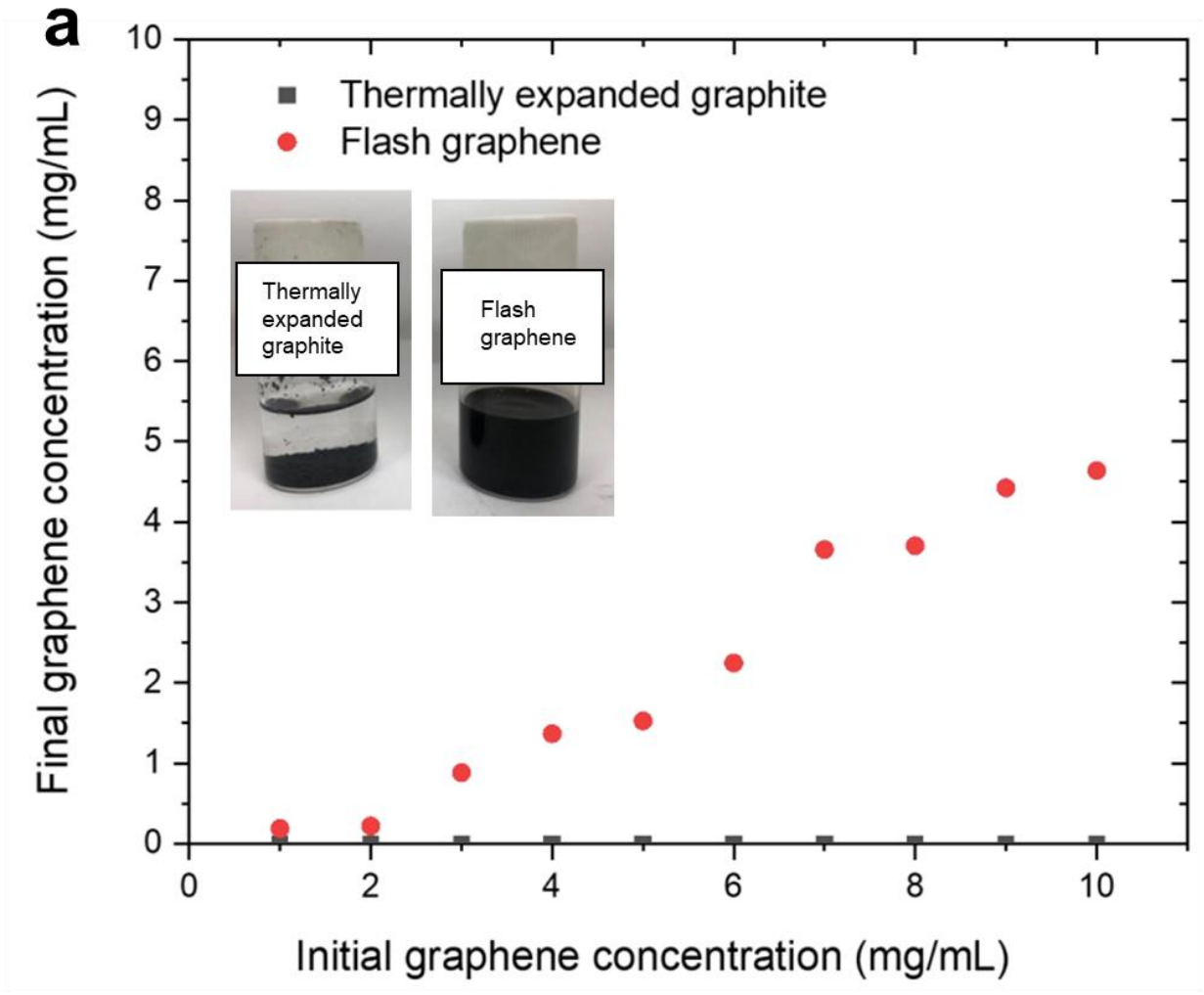
a
Thermally expanded graphite
Flash graphene
Thermally expanded graphite
Flash graphene
Final graphene concentration (mg/mL)
Initial graphene concentration (mg/mL)
0
1
2
3
4
5
6
7
8
9
10
0
2
4
6
8
10

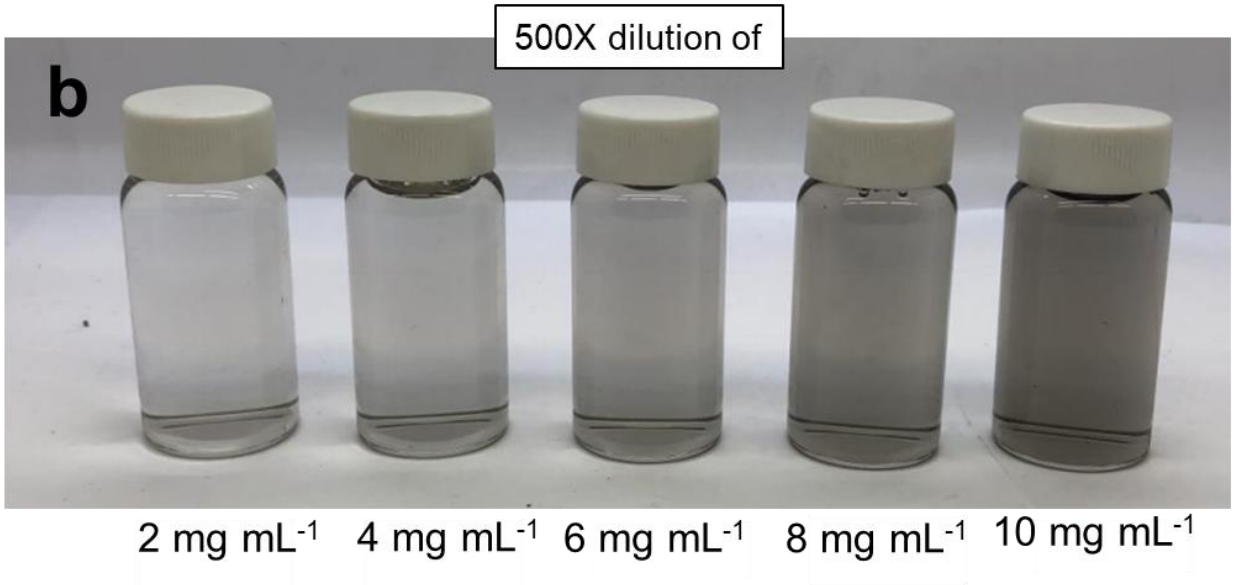
500X dilution of
b
2 mg mL-1
4 mg mL-1
6 mg mL-1
8 mg mL-1
10 mg mL-1

Supplementary Fig. 17. FG dispersion in water/Pluronic (F-127) (1%). a. Comparison of dispersibility of 5 mg mL^{-1} of thermally expanded graphite and CB-FG in water/Pluronic (F-127) (1%). The thermally expanded graphite settles after centrifugation (see Methods) while the CB-FG remains dispersed in the water surfactant solution. b. Visual dispersibility of CB-FG. The original concentration is specified below the image but that concentration was diluted 500x for visual demonstration of CB-FG dispersibility. No large particles are found visually in all diluted solutions.

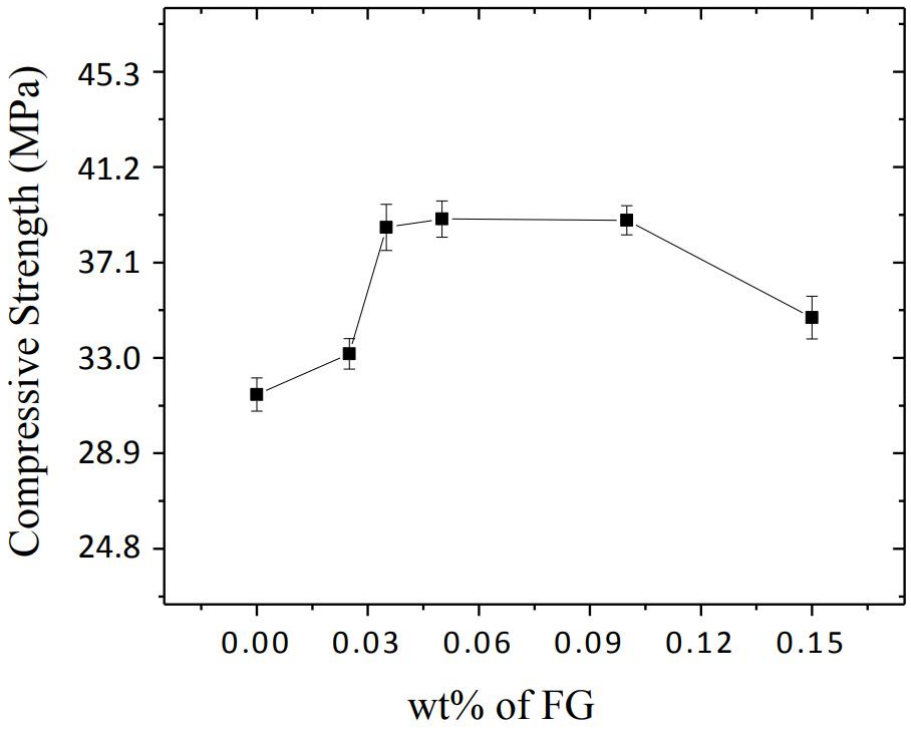

Supplementary Fig. 18. Mechanical properties of the CB-FG/cement composites measured at 28 days.

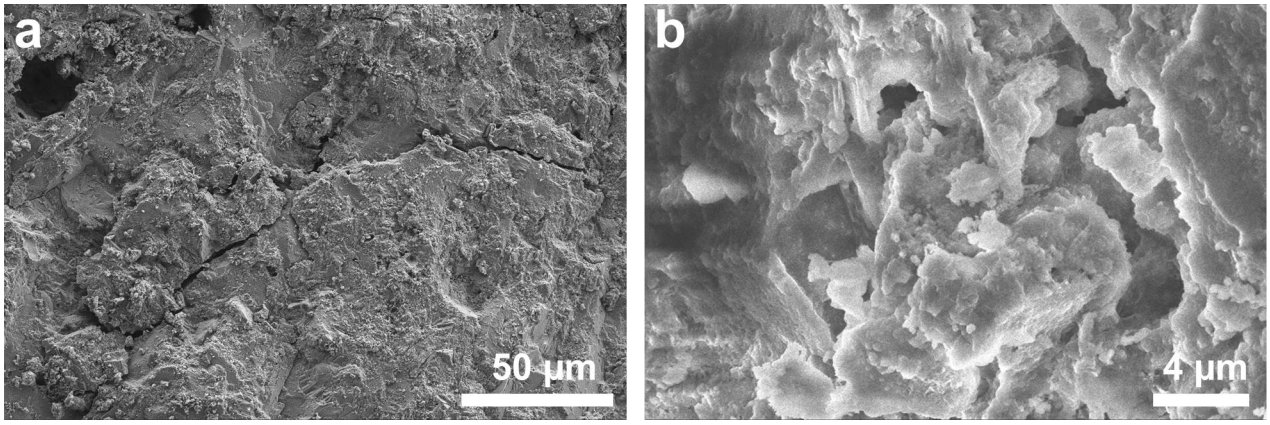

Supplementary Fig. 19. SEM images of cement and CB-FG composite. The SEM images show good graphene dispersion in Portland cement without any visible large flakes of graphene.

The large enhancement in the properties of CB-FG/cement composites could be due to the ease of dispersibility of the turbostratic CB-FG in water where the homogenously distributed sheet-like FG acts as templates to promote congruent growth of cement hydrate products.[31] Additionally, there is literature suggestion that covalent C-O bonds/networks between graphene and cement hydrate products can change the hybridization of graphene from sp^2 to sp^3 upon covalent bond formation, greatly enhancing the mechanical properties of the composite, though we cannot verify or substantiate the mechanism for that reaction.[32] It has been suggested that this change, along with electron release in the vicinity of their interfacial region, can lead to homogenous, inter-mixed and intercalated composites with improved properties. Whether this is taking place here has not been experimentally verified.

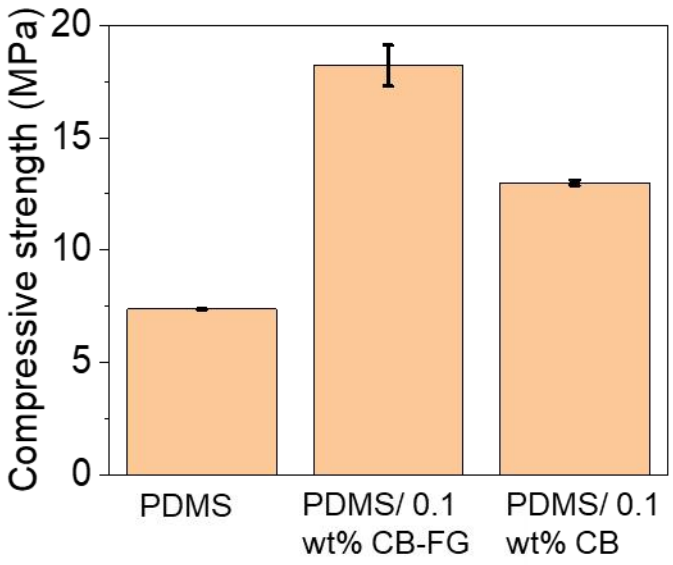

Supplementary Fig. 20. Compressive strength of PDMS, CB-FG/PDMS composite and CB/PDMS composite.

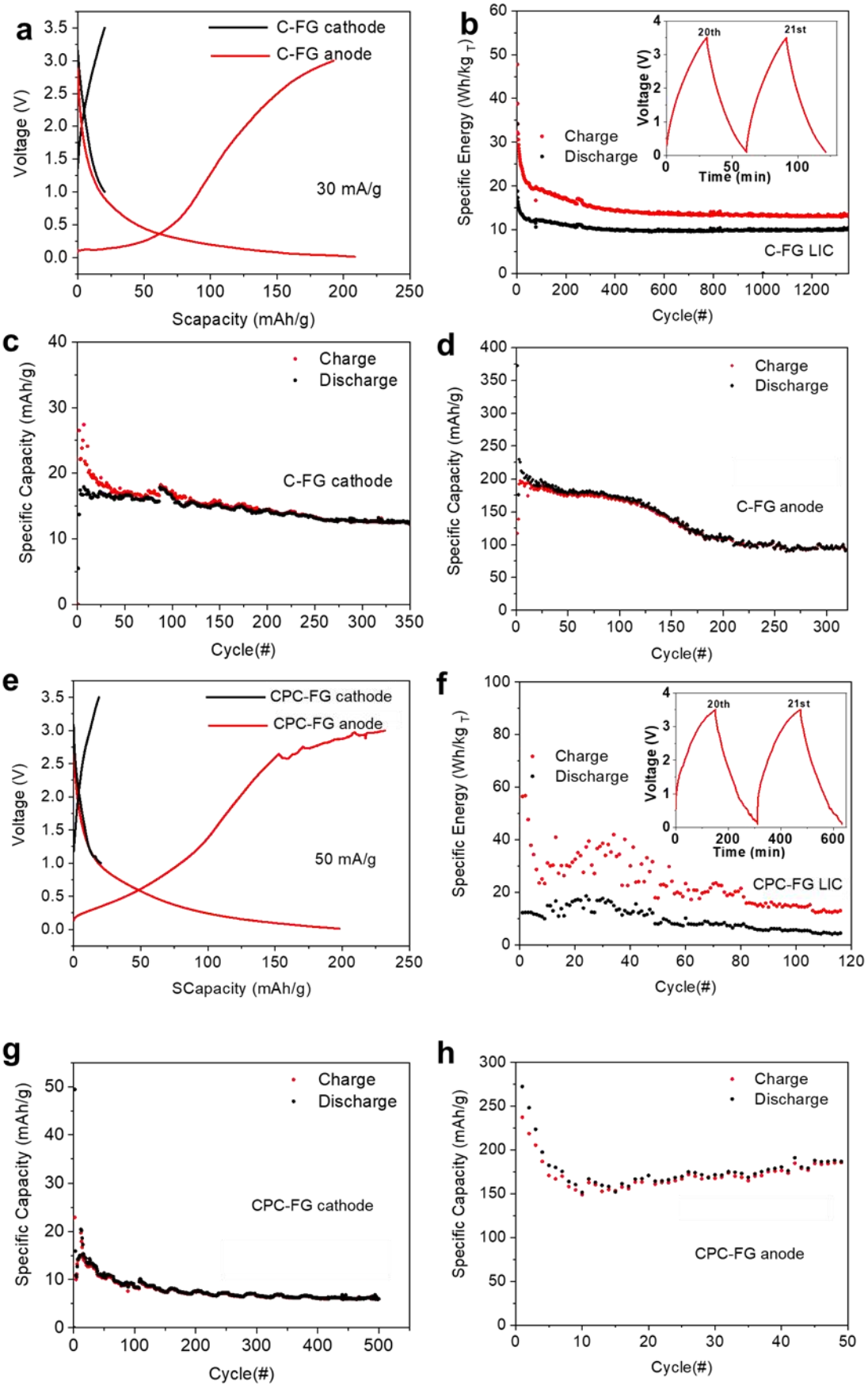
a
C-FG cathode
C-FG anode
30 mA/g
Voltage (V)
Scapacity (mAh/g)
b
Charge
Discharge
20th
21st
Voltage (V)
Time (min)
Specific Energy (Wh/kg T)
C-FG LIC
Cycle(#)
c
Charge
Discharge
C-FG cathode
Specific Capacity (mAh/g)
Cycle(#)
d
Charge
Discharge
C-FG anode
Specific Capacity (mAh/g)
Cycle(#)
e
CPC-FG cathode
CPC-FG anode
50 mA/g
Voltage (V)
SCapacity (mAh/g)
f
Charge
Discharge
20th
21st
Voltage (V)
Time (min)
Specific Energy (Wh/kg T)
CPC-FG LIC
Cycle(#)
g
Charge
Discharge
CPC-FG cathode
Specific Capacity (mAh/g)
Cycle(#)
h
Charge
Discharge
CPC-FG anode
Specific Capacity (mAh/g)
Cycle(#)

Supplementary Fig. 21. FG in a Li-ion capacitor and a Li-ion battery. A Li-ion battery was made and cycled, then the battery was opened and the anode and cathode were used to make the Li-ion capacitor. a. Charge/discharge curves of the Li-ion battery with C-FG anodes (0.01−3.0 V) and cathodes (1−3.5 V) in half-cells with Li foil as the counter and reference electrode. b. Long-range stability of C-FG Li-ion capacitor at 20 $mA.g^{-1}$. c. Cycling performance of the Li-ion battery with the C-FG cathode half-cell at 30 $mA.g^{-1}$. d. Cycling performance of the Li-ion battery with C-FG as the anode half-cell at 50 $mA.g^{-1}$. e. Charge/discharge curves of the Li-ion battery with calcined petroleum coke-FG (CPC-FG) anode (0.01−3.0 V) and cathode (1−3.5 V) in half-cells with Li foil as the counter and reference electrode. f. Long-range stability of the CPC-FG Li-ion capacitor at 5 $mA.g^{-1}$. g. Cycling performance of the Li-ion battery with CPC-FG as cathode at 25 $mA.g^{-1}$. h. Cycling performance of the Li-ion battery with CPC-FG as the anode half-cell at 100 $mA.g^{-1}$.

Electrochemical Test Protocols

The electrochemical performance of flashed graphene was tested in CR2032 cells. All the cells were assembled in a glove box under argon atmosphere. The CR2032 lithium-ion cell consists of lithium foil as the counter electrode, Celgard K2045 as the separator, 1 M lithium hexafluorphosphate (LiPF6) dissolved in 1:1:1 ethylene carbonate:dimethylcarbonate:diethylcarbonate (EC:DMC:DEC) (MTI corporation) as the electrolyte, and FG (C-FG and CC-FG) as cathode/anode. The cathode/anode were prepared by casting slurry which consists 80 wt% active material, 10 wt% (Super P, TIMCAL) and 10 wt% polyvinylidene difluoride (PVDF; Alfa Aesar) in *N*-methyl-2-pyrrolidone (NMP) on a piece of Al/Cu foil. The galvanostatic discharge/charge tests were carried out in voltage range of 0.01 to

3.0 V (vs Li+/Li) for anode and 1.0 to 3.5 V (vs Li+/Li) for cathode, respectively. The full capacitor performance of flashed graphene in the Li-ion capacitor was tested in CR2032 cells. In order to assemble the FG Li-ion capacitor, the anode and cathode of the Li-ion battery half-cells were cycled several times with the anode rested at the discharge state and cathode rested at the charge state. The two cells were opened inside a glovebox, re-assembled as a FG Li-ion capacitor, and tested in the voltage range of 0.1 to 3.5 V. The capacity of Li-ion capacitor was calculated based on the total mass of the anode plus cathode that had come from the Li-ion battery.

References

1 Novoselov, K. S. *et al.* Electric field effect in atomically thin carbon films. *Science* **306**, 666-669 (2004).

2 Allen, M. J. *et al.* Honeycomb carbon: a review of graphene. *Chem. Rev.* **110**, 132-145 (2009).

3 Partoens, B. & Peeters, F. M. From graphene to graphite: Electronic structure around the K point. *Phys. Rev. B* **74**, 075404 (2006).

4 Malard, L. M. *et al.* Raman spectroscopy in graphene. *Phys. Rep.* **473**, 51-87 (2009).

5 Bianco, A. *et al.* All in the graphene family – A recommended nomenclature for two-dimensional carbon materials. *Carbon* **65**, 1-6 (2013).

6 Yan, Z. *et al.* Hexagonal graphene onion rings. *J. Am. Chem. Soc.* **135**, 10755-10762 (2013).

7 Kim, K. *et al.* Raman spectroscopy study of rotated double-layer graphene: misorientation-angle dependence of electronic structure. *Phys. Rev. Lett.* **108**, 246103 (2012).

8 Kato, H. *et al.* Growth and Raman spectroscopy of thickness-controlled rotationally faulted multilayer graphene. *Carbon* **141**, 76-82 (2019).

9 Niilisk, A. *et al.* Raman characterization of stacking in multi-layer graphene grown on Ni. *Carbon* **98**, 658-665 (2016).

10 Kiselov, V. *et al.* The growth of weakly coupled graphene sheets from silicon carbide powder. *Semicond. Phys., Quantum Electron. Optoelectron.* 301-307 (2014).

11 Garlow, J. A. *et al.* Large-area growth of turbostratic graphene on Ni (111) via physical vapor deposition. *Sci. Rep.* **6**, 19804 (2016).

12 Ferrari, A. C. *et al.* Raman spectrum of graphene and graphene layers. *Phys. Rev. Lett.* **97**, 187401 (2006).

13 Novoselov, K. S. *et al.*Two-dimensional gas of massless Dirac fermions in graphene. *Nature* **438**, 197 (2005).

14 Ferrari, A. C. Raman spectroscopy of graphene and graphite: Disorder, electron–phonon coupling, doping and nonadiabatic effects. *Solid State Commun.* **143**, 47-57 (2007).

15 Kudin, K. N. *et al.* Raman spectra of graphite oxide and functionalized graphene sheets. *Nano Lett.* **8**, 36-41 (2008).

16 Ni, Z. H. *et al.* Probing Charged Impurities in Suspended Graphene Using Raman Spectroscopy. *ACS Nano* **3**, 569-574 (2009).

17 Ferrari, A. C. & Basko, D. M. Raman spectroscopy as a versatile tool for studying the properties of graphene. *Nat. Nano.* **8**, 235 (2013).

18 Kumar, N. *et al.* High-temperature phase transformation and low friction behaviour in highly disordered turbostratic graphite. *J. Phys. D: Appl. Phys.* **46**, 395305 (2013).

19. Yan, Zheng *et al.* Toward the Synthesis of Wafer-Scale Single-Crystal Graphene on Copper Foils. *ACS Nano* **6**, 9110-9117 (2012).

20. Franklin, R. E. Crystallite growth in graphitizing and non-graphitizing carbons. *Proc. R. Soc. Lond. A.* **209**, 196-218 (1951).

21. Harris, P. J. F. & Tsang, S. C. High-resolution electron microscopy studies of non-graphitizing carbons. *Philos. Mag. A* **76**, 667-677 (1997).

22. Iijima, S. Direct observation of the tetrahedral bonding in graphitized carbon black by high resolution electron microscopy. *J. Cryst. Growth* **50**, 675-683 (1980).

23. Huang, J. Y. *et al.* Real-time observation of tubule formation from amorphous carbon nanowires under high-bias Joule heating. *Nano Lett.* **6**, 1699-1705 (2006).

24. Wang, B. *et al.* Electro-graphitization and exfoliation of graphene on carbon nanofibers. *Carbon* **117**, 201-207 (2017).

25. Vander Wal, R. L. *et al.* Carbon nanostructure examined by lattice fringe analysis of high-resolution transmission electron microscopy images. *Appl. Spectrosc.* **58**, 230-237 (2004).

26. Kim, D.-Y., Nishiyama, Y., Wada, M. & Kuga, S. Graphitization of highly crystalline cellulose. *Carbon* **39**, 1051-1056 (2001).

27. Haensel, T. *et al.* Pyrolysis of cellulose and lignin. *Appl. Surf. Sci.* **255**, 8183-8189 (2009).

28. Luo, B. *et al.* Chemical vapor deposition of bilayer graphene with layer-resolved growth through dynamic pressure control. *J. Mater. Chem. C* **4**, 7464-7471 (2016).

29. Li, J. *et al.* Controllable atmospheric pressure growth of mono-layer, bi-layer and tri-layer graphene. *Chem. Commun.* **50**, 11012-11015 (2014).

30. Jalilov, A. S. *et al.* Mechanistic study of the conversion of superoxide to oxygen and hydrogen peroxide in carbon nanoparticles. *ACS Appl. Mater. Interfaces* **8**, 15086-15092 (2016).

31. Moghaddam, S. E. *et al.* Morphogenesis of cement hydrate. *J. Mater. Chem. A* **5**, 3798-3811 (2017).

32. Hosseini, E., Zakertabrizi, M., Korayem, A. H. & Shahsavari, R. Tunable, multifunctional ceramic composites via intercalation of fused graphene boron nitride nanosheets. *ACS Appl. Mater. Interfaces* **11**, 8635-8644 (2019).